IEEE Access
Multidisciplinary | Rapid Review | Open Access Journal

Date of publication xxxx 00, 0000, date of current version xxxx 00, 0000.

Digital Object Identifier 10.1109/ACCESS.2021.Doi Number

The IEEE-SA Working Group on Spaceborne GNSS-R: Scene Study

Hugo Carreno-Luengo[1], Senior Member, IEEE, Adriano Camps[2,3], Fellow Member, IEEE, Chris Ruf[1], Fellow Member, Nicolas Floury[4], Manuel Martin-Neira[4], Senior Member, IEEE, Tianlin Wang[1], Student Member, IEEE, Siri Jodha Khalsa[5], Senior Member, IEEE, Maria Paola Clarizia[6], Senior Member, IEEE, Jennifer Reynolds[6], Joel Johnson[7], Fellow Member, IEEE, Andrew O'Brien[7], Member, IEEE, Carmela Galdi[8], Member, IEEE, Mauricio di Bisceglie[8], Member, IEEE, Andreas Dielacher[9], Philip Jales[10], Martin Unwin[11], Lucinda King[12], Giuseppe Foti[13], Rashmi Shah[14], Senior Member, IEEE, Daniel Pascual[6], Member, IEEE, Bill Schreiner[15], Milad Asgarimehr[16], Jens Wickert[16,17], Serni Ribo[3,18], Member, IEEE, Estel Cardellach[3,18], Senior Member, IEEE

[1]Climate and Space Sciences and Engineering Department, University of Michigan (UM), Ann Arbor, MI, United States of America
[2]CommSensLab-UPC, Universitat Politecnica de Catalunya (UPC), Barcelona, Spain
[3]Instiut d'Estudis Espacials de Catalunya (IEEC), Barcelona, Spain
[4]European Space Research and Technology Center (ESTEC)/European Space Agency (ESA), Noordwijk, The Netherlands
[5]National Snow and Ice Data Center (NSIDC), University of Colorado, Boulder, CO, United States of America
[6]Deimos Space UK Ltd., Harwell, United Kingdom
[7]Electrical and Computer Engineering, The Ohio State University, Columbus, OH, United States of America
[8]Dipartimento di Ingegneria, Universita degli Studi del Sannio, Benevento, Italy
[9]RUAG Space GmbH, Vienna, Austria
[10]Spire Global, Boulder, CO, United States of America
[11]Surrey Satellite Technology Ltd. (SSTL), Guildford, United Kingdom
[12]University of Surrey, Surrey, United Kingdom
[13]National Oceanography Center (NOC), Southampton, United Kingdom
[14]Jet Propulsion Laboratory (JPL)/California Institute of Technology, Pasadena, CA, United States of America
[15]University Corporation for Atmospheric Research, Boulder (UCAR), CO, United States of America
[16]German Research Centre for Geosciences (GFZ), Potsdam, Germany
[17]Technische Universität Berlin (TUB), Berlin, Germany
[18]Institute of Space Sciences (ICE), Barcelona, Spain

Corresponding author: Hugo Carreno-Luengo (carreno@umich.edu).

This research was supported in part by the NASA Science Mission Directorate contract NNL13AQ00C with the University of Michigan.

ABSTRACT The Institute of Electrical and Electronics Engineers (IEEE) Geoscience and Remote Sensing Society (GRSS) created the GRSS "Standards for Earth Observation Technical Committee" to advance the usability of remote sensing products by experts from academia, industry, and government through the creation and promotion of standards and best practices. In February 2019, a Project Authorization Request was approved by the IEEE Standards Association (IEEE-SA) with the title "Standard for Spaceborne Global Navigation Satellite Systems Reflectometry (GNSS-R) Data and Metadata Content."

At present, 4 GNSS constellations cover the Earth with their navigation signals: The United States of America (USA) Global Positioning System GPS with 31 Medium Earth Orbit (MEO) operational satellites, the Russian GLObal'naya NAvigatsionnaya Sputnikovaya Sistema GLONASS with 24 MEO operational satellites, the European Galileo with 24 MEO operational satellites, and the Chinese BeiDou-3 with 3 Inclined GeoSynchronous Orbit (IGSO), 24 MEO, and 2 Geosynchronous Equatorial Orbit (GEO) operational satellites. Additionally, several regional navigation constellations increase the number of available signals for remote sensing purposes: the Japanese Quasi-Zenith Satellite System QZSS with 1 GSO and 3 Tundra-type orbit operational satellites, and the Indian Regional Navigation Satellite System IRNSS with 3 GEO and 4 IGSO operational satellites. On the other hand, there are different GNSS-R processing techniques, instruments and spaceborne missions, and a wide variety of retrieval algorithms have been used.

The heterogeneous nature of these signals of opportunity as well as the numerous working methodologies justify the need of a standard to further advance in the development of GNSS-R towards an operational Earth Observation technique. In particular, the scope of this working group is to develop a standard for data and metadata content arising from past, present, and future spaceborne missions such as the United

This article has been accepted for publication in a future issue of this journal, but has not been fully edited. Content may change prior to final publication. Citation information: DOI 10.1109/ACCESS.2021.3089762, IEEE Access

Kingdom (UK) TechDemoSat-1 TDS-1, and the National Aeronautics and Space Administration (NASA) CYclone Global Navigation Satellite System CYGNSS constellation coordinated by the University of Michigan (UM). In this article we describe the scene study, including fundamental aspects, scientific applications, and historical milestones. The spaceborne standard is under development and it will be published in IEEE-SA.

INDEX TERMS GNSS-R, IEEE Standards Association, Satellite Missions, Earth Remote Sensing

I. OVERVIEW OF THE IEEE STANDARD FOR SPACEBORNE GNSS-REFLECTOMETRY

A. INTRODUCTION TO THE STANDARD: STRUCTURE AND CONTENTS

This working group has been assembled to develop this standard with the purpose of unifying and documenting GNSS-R measurements, calibration procedures, and product level definitions (https://standards.ieee.org/). It includes members, collaborators, and contributors from academia, international space agencies, and private industry. In a face-to-face meeting held on November 2019 during the 6th Workshop on Advanced RF Sensors and Remote Sensing Instruments (ARSI'19) and 4th Ka-band Earth Observation Radar Missions Workshop (KEO'19) joint meeting, the need was recognized to develop a standard with a wide range of operations, providing procedure guidelines independently of constraints imposed by current limitations on geophysical parameters retrieval algorithms. As such, this effort aims to establish the fundamentals of a potential virtual network of satellites providing inter-comparable data to the scientific community (Figs. 1,2).

The proposed IEEE standard [1] presented hereafter has been submitted under the sponsorship of GRSS and is limited to GNSS-R [2-5]. The IEEE standard was first presented in the 2020 IEEE International Geoscience and Remote Sensing Symposium (IGARSS). Here it is summarized, and it is used as the base of this paper. The primary objectives of the standard are three-fold:

a) To define a comprehensive, accurate, and clear set of low-level parameters that forms a standard product. The choice of parameters shall be sufficient to enable the accurate retrieval of at least the most common GNSS-R products: Ocean wind speed and surface altimetry, Soil Moisture Content (SMC), Above-Ground Biomass (AGB), inland water, and sea ice.

b) To define the procedures that shall be followed to generate the required fundamental and derived observables that configure this standard: Estimation of the nominal specular point, absolute power calibration, correction for path and atmospheric delays in phase, impact of the coherent scattering term in the bistatic radar cross section, estimation of the scattering area, computation of the noise floor, and

FIGURE 1. Artist's view of the UK-TDS-1 satellite. Image credits Surrey Satellite Technology Ltd. (SSTL).

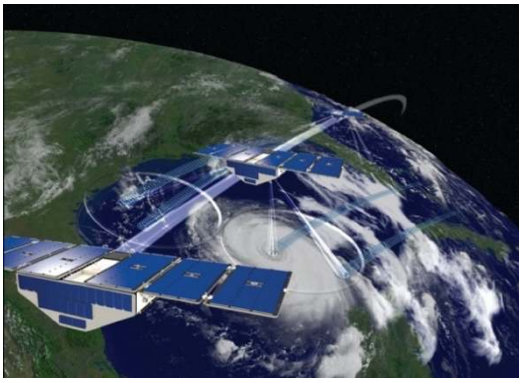

FIGURE 2. Artist's view of the NASA's CYGNSS constellation coordinated by the University of Michigan (UM). Image credits NASA.

Radio Frequency Interference (RFI) detection and mitigation.

c) To generate a list of metadata and quality flags that provide as much information as possible to the final users.

B. THE MOST GENERIC GNSS-R OBSERVABLE: THE DELAY DOPPLER MAP

The basic GNSS-R observables are the so-called delay-waveforms and Delay Doppler Maps (DDMs) (Fig. 3). Some GNSS reflectometers provide only power waveforms. Some others are able to deliver their in-phase I and quadrature Q components, and thus providing phase information of the reflected electromagnetic field. The most widely used GNSS-R observable is the power DDM. Power DDMs $\left\langle |Y_r(\tau,f)|^2 \right\rangle$ can be modelled using geometrical and scattering related parameters as follows [4]:

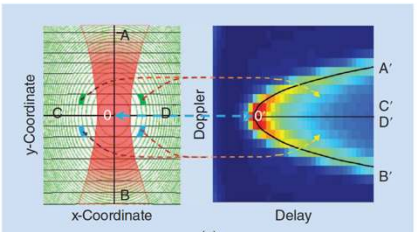

FIGURE 3. Sketch of a sample Delay-Doppler Map (DDM) [4].

$$\left\langle \left|Y_r(\tau,f)\right|^2 \right\rangle = \frac{T_c^2 P_T \lambda^2}{(4\pi)^3} \iint \frac{G_T G_R \left|\chi(\tau-(R_T+R_R)/c, f-f_c)\right|^2 \sigma^0}{R_T^2 R_R^2} d^2\bar{\rho}, \quad (1)$$

where T_c is the coherent integration time, P_T is the power of the transmitted signals, λ is the wavelength of the signals, G_T and G_R are the transmitting and receiving antenna gains towards the direction of the reflected radio-link, R_T and R_R are the ranges from the transmitter and the receiver to the specular point, respectively, χ is the Woodward Ambiguity Function (WAF), τ is the delay of the signal from the transmitter to the receiver, f is the Doppler shift of the reflected signal, f_c is aimed to compensate the Doppler shift of the signal, σ^0 is the bistatic scattering coefficient, and $\bar{\rho}$ is the positioning vector of the scattering point on the reflecting area.

The bistatic scattering coefficient can be defined as follows [6-9]:

$$\sigma^0 = \sigma^{coh,0} + \sigma^{incoh,0}, \quad (2)$$

where $\sigma^{coh,0}$ and $\sigma^{incoh,0}$ are the coherent and the incoherent scattering terms respectively. Consequently, DDMs consist of a sum of two terms as follows [6-9]:

$$\left\langle \left|Y_r(\tau,f)\right|^2 \right\rangle = \left\langle \left|Y_{r,coh}(\tau,f)\right|^2 \right\rangle + \left\langle \left|Y_{r,incoh}(\tau,f)\right|^2 \right\rangle. \quad (3)$$

$\left\langle \left|Y_{r,coh}(\tau,f)\right|^2 \right\rangle$ accounts for coherent reflections from the surface, while $\left\langle \left|Y_{r,incoh}(\tau,f)\right|^2 \right\rangle$ is responsible for the diffuse scattering.

$\left\langle \left|Y_{r,coh}(\tau,f)\right|^2 \right\rangle$ can be expressed analytically for the case of an infinite and homogeneously reflecting surface as follows [6-9]:

$$\left\langle \left|Y_{r,coh}(\tau,f)\right|^2 \right\rangle = \frac{T_c^2 P_T \lambda^2 G_T G_R \left|\chi(\tau,f)\right|^2}{(4\pi)^2 (R_T+R_R)^2} \left|R(\theta_i)\right|^2 \gamma \exp(-(2k\sigma\cos\theta_i)^2), \quad (4)$$

where R is the Fresnel reflection coefficient, k is the signal angular wavenumber, σ is the surface height standard deviation (related to small-scale surface roughness), γ is the transmissivity of the vegetation, and θ_i is the incidence angle.

$\left\langle \left|Y_{r,incoh}(\tau,f)\right|^2 \right\rangle$ includes contributions from vegetation, small-scale surface roughness, and topography. Further details on the incoherent scattering over rough surfaces can be found in [4]. The impact of attenuation and scattering by the upwelling vegetation should be considered to establish an accurate model of the incoherently scattered field.

More recently, a new model capable of evaluating both the incoherent and the coherent scattering terms [10] has been developed based on aperture diffraction theory. It has been validated over a lake with spaceborne data as generated using the CYGNSS raw Intermediate Frequency (IF) processor. This model is helpful for accurate analysis of composite scattering from smaller smooth regions interspersed in larger rough terrain.

C. DATA PRODUCTS

An outline of the data products is provided here. Different techniques with a spaceborne application are considered including conventional c-, interferometric i-, reconstructed r-, and partial interferometric pi- GNSS-R. All the complete definitions and details are part of the "Standard for Spaceborne Global Navigation Satellite System-Reflectometry (GNSS-R) Data and Metadata Content" [11].

1) FUNDAMENTAL OBSERVABLES

The following fundamental observables are required to be in agreement with the standard:

• ddm_complex: This field includes the after-correlation in-phase I (real part) and quadrature Q (imaginary part) components of the scattered signal in raw counts. GNSS-R sensors of the c- and r-type shall ideally provide two ddm_complex observables, one for the direct and one for the reflected signal. The GNSS-R sensors of the i-type only need to produce one ddm_complex measurement. The nominal specular point location may be accurately and efficiently computed using e.g. the DTU 10 model over ocean and e.g. the MERIT or Earth 2014 Digital Elevation Model (DEM) over land (or a "reduced" version of these models). Over land, several specular reflection points may be encountered. The number will depend on facet size, but on surface roughness as well, as it widens the angular pattern of the scattered signal [4]. If it is too rough, the pattern will be too wide, and it will not be coherent anymore. These considerations lead to the fundamental question of how to define the specular point: minimum delay?, incidence angle of the incident wave equals incidence angle of the reflected wave? The array size shall be sufficiently large to account for the complete spreading of the DDMs in delay and Doppler domains. State-of-the-art values are ~ 4 GPS Coarse Acquisition (C/A) chips x 5000 Hz or ~ 30 GPS C/A chips x 10000 Hz for the C/A code systems. The optimum delay and Doppler bins size are also being analyzed. The bin size shall be defined considering the scientific requirements versus the peak uncertainty. Coherent integration time shall be assumed to

be a variable. All information defining the processing approach shall be included as metadata. It is recommended to study the possibility of using direct and reflected signals synchronized in the same correlation channel for system autocalibration.

• ddm_complex_compressed: This is the compressed ddm_complex, i.e. the ddm_complex variable compressed to reduce the number of bits required in its representation. The selected compression approach and any uncertainties introduced shall be included in metadata.

• ddm_complex_cal: This is the calibrated ddm_complex after the application of any corrections for calibration purposes. The calibration method shall be included in the metadata.

• ddm_complex_compressed_cal: This is the calibrated ddm_complex_compressed, after the application of any corrections for calibration purposes. The calibration method shall be included in the metadata.

• ddm_power: This is the uncalibrated power value in raw counts, that is, the squared modulus of ddm_complex or ddm_complex_compressed. The incoherent integration time shall be assumed to be a variable. Default-values for land and ocean surfaces shall be specified for each type of surface. These values shall be included in the nominal operational mode of the receiver. The location of the specular point corresponding to the ddm_power shall be identified. This information shall be included as metadata. ddm_power observables may be produced on-board but also on-ground.

• ddm_power_cal: This is the calibrated power that would have been measured by an ideal GNSS-R sensor. An ideal GNSS-R sensor is one with isotropic antennas and known instrumental gain, delays and offsets, having no quantization errors. Calibration procedures both in delay and amplitude shall be defined including those for cGNSS-R, iGNSS-R, rGNSS-R, and piGNSS-R. Different options exist for calibration. Direct and reflected signals may be routed to a calibration switch circuit inserted between them and their Low Noise Amplifiers (LNAs) which allows for accurate delay and amplitude calibration. Other calibration approaches are possible, including the injection of Pseudo-Random Noise (PRN) signals or using the same antenna for direct and reflected signal. The calibration method shall be included in the metadata.

• phase: This value is the phase [deg] of the calibrated complex (ddm_complex_cal or ddm_complex_compressed_cal) DDMs. The point of the DDMs to what this value corresponds shall be included in metadata. It can be the peak (totally coherent scattering) or the point of maximum derivative of the leading edge of the delay-waveforms (coherent and incoherent scattering terms exist). In the case of GNSS-R sensors of the c- and r-type, phase shall include both direct and reflected correlation channels. The phase shall be corrected for path and atmospheric delays. Such correction shall be also included in the metadata. Note: The use of model based open loop tracking (delay, Doppler) allows phase retrieval without a full waveform sampling [12,13].

• power: This value is the peak power of the calibrated complex (ddm_complex_cal or the ddm_complex_compressed_cal) and calibrated power (ddm_power_cal) DDMs. In the case of GNSS-R sensors of the c- and r- type the power shall include both direct and reflected correlation channels. The power unit shall be [dBm]. Automatic Gain Control (AGC) shall be stable, and it is recommended to remove any AGC influence by using a constant gain channel.

2) DERIVED OBSERVABLES

The following derived observables are required to be in agreement with the standard:

• brcs: This is the bistatic scattering radar cross section [m^2]. The impact of any coherent scattering term shall be separated. This term shall be also considered for the computation of the overall path loses. The level of the reflected signal relative to the direct signal shall be accurately estimated using preferably the direct signals themselves instead of a look-up table. The GNSS satellites antenna radiation pattern in the direction of the up-looking antenna and the specular point may be assumed to be similar or estimated.

• effective_area: This is an estimate of the effective surface scattering area [m^2] that contributes in terms of power to each DDM bin, after accounting for the GNSS signal spreading function. It may be calculated by convolving the GNSS WAF with the surface area that contributes in terms of power to a given DDM bin as determined by its delay and Doppler values and the measurement geometry. The specular point bin location matches the specular point bin location in the brcs. State-of-the art procedures use an "end-to-end simulator" such as the CYGNSS or the PAU/PARIS simulator. This information shall be included as a look-up table.

• nbrcs: This value is an estimation of the normalized bistatic scattering radar cross section [dB] derived from dividing brcs by effective_area. For wind speed retrieval, a window of delay and Doppler bins centered in the nominal specular point corresponding to the nominal spatial resolution on Earth's surface should be used (typically) ~ 25 km x 25 km for systems using the L1 C/A code (3 delay and 5 Doppler bins in CYGNSS). This window size may be assumed to be a variable, and information shall be included as metadata.

• snr: This value is the Signal-to-Noise Ratio (SNR) of the power DDMs, taking the level of noise floor as reference, in [dB]. In the case of GNSS-R sensors of the c- and r-type, snr shall include both direct and reflected correlation channels.

• noise_floor: This value is the noise floor of the complex (ddm_complex or ddm_complex_compressed) and power (ddm_power) DDMs. In the case of GNSS-R sensors of the

c- and r-type, noise_floor shall include both direct and reflected correlation channels. The units of the n_floor are arbitrary units. The computation of n_floor shall account for the type of surface i.e. ocean vs. land, including the effect of topography if needed. It shall be computed as the average over the number of bins before beginning of the leading edge, for all Doppler frequencies in the DDM.

• gamma: This value is the reflectivity computed from the calibrated power (ddm_power_cal) DDMs [dB]. The use of an empirical estimation has been evaluated because both the coherent and the incoherent scattering terms contribute to the peak power of the DDMs [4,9].

• area and vol: This is the area (area) and the volume (vol) of calibrated power (ddm_power_cal) DDMs. In the case of GNSS-R sensors of the c- and r-type, area_vol shall include both direct and reflected correlation channels. Simulation work indicates that the volume and the area of the DDMs are related to the changes in the contribution to the brightness temperature of the ocean induced by the roughness.

• te and le: This value is the trailing & leading edges width of calibrated power (ddm_power_cal) DDMs in [m]. It is defined as the lag difference between a certain power threshold of the reflected power delay waveforms and the corresponding maximum power of the waveforms. In the case of GNSS-R sensors of the c- and r-type the te and le shall include both direct and reflected correlation channels. The power threshold information shall be included as metadata.

• del: This value is the delay between the peak of the direct power delay waveforms and the point of maximum derivative of the reflected power delay waveforms.

• coh_to_incoh: This value is the coherent-to-incoherent scattering ratio [4,6].

• coh_comp: This is the coherent component of calibrated power (ddm_power_cal) DDMs. “Coherent DDMs” can be generated after removing the influence of the incoherent scattering term by the computation of the variance of the coherently integrated DDMs prior to the incoherent averaging.

II. GNSS-R TECHNIQUES

It is understood that there are several different techniques for producing spaceborne GNSS-R measurements, and it is the intention of the working group that the standard will be applicable generally to all of them. The working group has identified, presently, the 4 current or proposed GNSS-R techniques used in spaceborne applications:

A. CONVENTIONAL GNSS-R

Conventional GNSS-R (cGNSS-R) (Fig. 4) [5,14-17] correlates coherently during Tc (typically 1 ms for GPS L1 C/A, L5 and Galileo E5; and 4 ms for Galileo E1 OS) the reflected signal with a locally generated replica of the

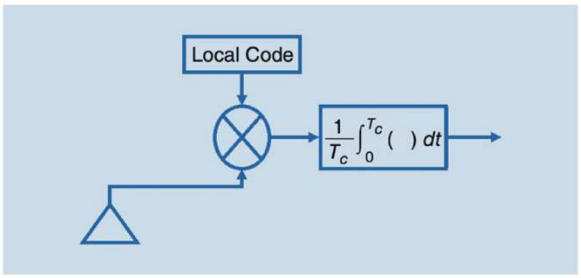

FIGURE 4. Basic concept of a conventional GNSS-R instrument [4].

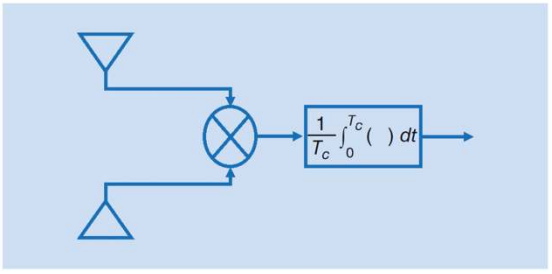

FIGURE 5. Basic concept of an interferometric GNSS-R instrument [4].

transmitted signal after proper compensation of the Doppler frequency shift, possibly for a number of Doppler frequencies around the central Doppler and/or time delays. cGNSS-R can be used even from platforms with small antennas and relatively low coherent and incoherent integration times. As such, this technique is recommended for land surfaces applications (e.g. soil moisture and biomass monitoring) because of the higher spatial resolution as compared to iGNSS-R (explained in the following) that requires longer integration times because of the lower SNR (unless very large and directive antennas are used).

B. INTERFEROMETRIC GNSS-R

In the interferometric GNSS-R (iGNSS-R) case [5,14] (Fig. 5) the reflected signal is cross-correlated with a measured direct signal itself after proper Doppler frequency and delay adjustment. iGNSS-R allows exploiting the full spectral density of the GNSS signals (i.e. all the codes are implicitly available, even the encrypted ones), thus improving ranging precision because of the steeper slope of the power waveforms on the tracking point (the point of maximum slope in the leading edge). As such, iGNSS-R can provide enhanced precision in ocean altimetry as compared to cGNSS-R using only the publicly available codes. On the other hand, the SNR [18,19] is a key-parameter because thermal noise affects both the direct and reflected signal measurements, and the noise of the cross-correlation signal is severely degraded unless the size of the up- and down-looking antennas is increased significantly. Consequently, beam-steering techniques and eventually multi-beam antennas (1 per Space Vehicle SV to be tracked

This article has been accepted for publication in a future issue of this journal, but has not been fully edited. Content may change prior to final publication. Citation information: DOI 10.1109/ACCESS.2021.3089762, IEEE Access

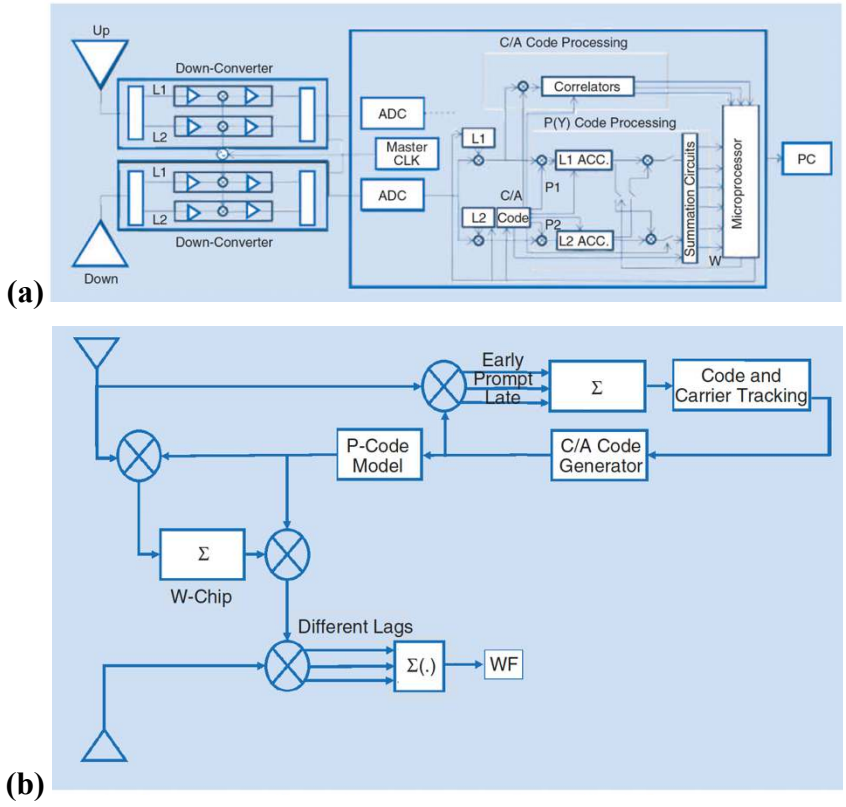

FIGURE 6. **Basic approaches of the reconstructed GNSS-R technique: (a) adapted from [4,27] and (b) adapted from [4,28].**

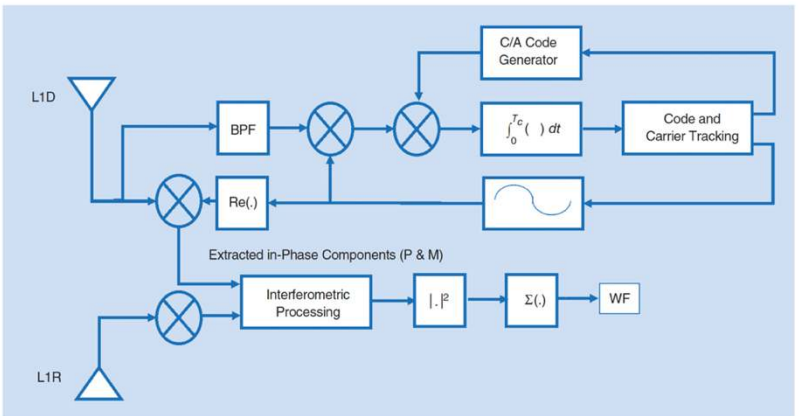

FIGURE 7. **Basic approach of the partial interferometric GNSS-R technique (adapted from [4,29]).**

and 1 for its corresponding reflection) are required to guarantee a high spatio-temporal sampling of the surface for mesoscale altimetry. Additionally, a proper calibration process is required to improve the altimetric product accuracy because of instrument thermal and aging drifts. However, a self-calibrated configuration can be used to compensate for these drifts. The Passive Reflectometry and Interferometry System In-orbit Demonstration (PARIS IoD) [14], the GNSS REflectometry, Radio Occultation, and Scatterometry Onboard the International Space Station (GEROS-ISS) [20], and the GNSS Transpolar Earth Reflectometry exploriNg System (G-TERN) [21] Phase A studies, the "Cookie" [22] concept, and several additional works [23-25] provide results on the performance of iGNSS-R design. It should be pointed out that this optimization does not apply to a cGNSS-R altimeter, since there is only a down-looking antenna and receiving channel, and any drifts in the frequency response, immediately translate into a delay error that cannot be compensated for.

C. RECONSTRUCTED CODE GNSS-R

Reconstructed-code GNSS-R (rGNSS-R) [27,28] (Fig. 6) is similar to the cGNSS-R technique, but semi-codeless techniques are used to reconstruct the P(Y) or other codes which are then correlated with the reflected signal. In [27], the correlation approach used in the down-looking channel instrument provides P-code processing of encrypted GPS signals without knowledge of the encrypted code, in addition to the C/A code for cGNSS-R, while the up-looking channels use a similar correlation approach and feed the information to the down-looking channel. In [28], the direct L1 C/A signal is processed with typical Delay Locked Loops (DLLs) and Phase Locked Loops (PLLs). The locked C/A code model is used to form a L1 P model, which is then applied to the direct signal, and after integration over ~ 0.5 MHz W-chips to estimate their signs, it is combined with the P-code model to form a L1 Y-code model which is used to correlate with the down-looking channel. The advantages of rGNSS-R rely mainly on the larger bandwidth of the P(Y) codes as compared to the C/A ones, and the larger SNR as compared to iGNSS-R, despite the losses of the semi-codeless approach.

D. PARTIAL INTERFEROMETRIC GNSS-R

Partial interferometric GNSS-R (iGNSS-R) [29] (Fig. 7) is similar to the iGNSS-R technique but using only as reference signal the encrypted large-bandwidth signals (P and M code components) of the direct signal. Although the signal bandwidth is the same, the Gabor bandwidth is larger, and so is the achievable range resolution as compared to the iGNSS-R. However, this theoretical improvement comes at the expense of a 3 dB signal loss as the C/A code has been removed, which has to be compensated by a 3 dB larger antenna directivity.

E. COMPARISON OF DIFFERENT TECHNIQUES

At present, cGNSS-R is the most widely used technique. iGNSS-R provides an improved accuracy in ocean altimetry products but requires higher directivity in both the up- and down- looking antennas. On the other hand, instruments of the i-type are much more complex and require a dedicated calibration strategy. However, tracking and re-tracking strategies are of lower complexity because of the lower dynamics as compared to cGNSS-R [30,31]. In general, the best SNR performance (which could turn into best altimetric performance) is the one given by rGNSS-R. The improvement between the altimetric performance of the iGNSS-R technique with respect to the one achieved by cGNSS-R (C/A code) is at least a factor of 2 [24]. Further studies are required to elucidate the pros and cons of the different techniques for the different scientific applications, including ocean, land, and cryosphere.

III. GNSS-R MISSIONS AND INSTRUMENTS

In defining the GNSS-R standard, a top priority is that it will be applicable to the wide range of past e.g. UK TDS-1 (Fig. 1), present e.g. NASA CYGNSS (Fig. 2), and future spaceborne GNSS-R missions (Table I), but also to ground-based and airborne instruments (Table II). In this Section, an overview of the key-parameters of these missions and instruments is provided, including information about the GNSS-R technique, band, polarization, and GNSS system used by the different satellites and instruments.

At present, the most common configuration is [cGNSS-R, L1/LHCP, GPS]. UK TDS-1 [2] and CYGNSS [3] use this configuration, although different signals can also be processed using raw collections of IF samples. BuFeng-1 A/B also follow this configuration, but additionally can collect BeiDou signals [36].

UK TDS-1 (Fig. 1) was launched into space in 2015 with 8 payloads on-board. One of these payloads was a technology demonstrator GNSS-R instrument [33]. UK TDS-1 data were publicly available. As such, the community was able to check and to develop new retrieval algorithms. CYGNSS (Fig. 2) has been the first operational GNSS-R mission launched into space. CYGNSS was first proposed for ocean wind speed estimation over tropical cyclones, although it has been extended to operations over land surfaces. The orbital configuration of each CYGNSS satellites is a circular Low Earth Orbit (LEO) with a height of ~ 520 km and an inclination angle of ~ 35°. At present, all 8 CYGNSS spacecrafts are healthy and operating nominally [56]. More recently, BuFeng-1 A/B twin satellites were also launched into space. Each platform has 2 Nadir GNSS-R antennas, 1 navigation antenna, 1 auxiliary antenna, 4 LNAs with blackbody calibration, and a GNSS-R receiver. The two Nadir antennas are directed at the left and right sides of the platform with inclination angles of ~ 26°. A first feasibility study for wind speed retrieval has been performed [36].

Finally, it is highlighted that ^{3}Cat-2 [34], launched in 2016, was the first CubeSat mission dedicated to GNSS-R. More recently, more CubeSats have also been launched [37,39].

IV. SCIENTIFIC APPLICATIONS

There are several scientific applications of GNSS-R for different surface types including ocean, land, and cryosphere. This Section provides an overview of the most relevant algorithms, as well as the associated GNSS-R techniques.

A. OCEAN

GNSS Earth-reflected signals can be used as sources of opportunity for mesoscale ocean altimetry and wind speed retrieval with improved spatio-temporal sampling as compared to traditional monostatic radar altimetry and scatterometry.

1) OCEAN ALTIMETRY

The potential of c/iGNSS-R for ocean altimetry (Fig. 8) was first published in 1993 [5]. Over smooth ocean

TABLE I. GNSS-R space-borne missions. Left- and Right- Hand Circular Polarization (L, R- HCP).

Mission	Date	GNSS-R type	Band/Pol used	GNSS used
UK-DMC [32]	2003	cGNSS-R	L1 / LHCP	GPS
UK-TDS-1 [33]	2015	cGNSS-R	L1 / LHCP	GPS
CYGNSS [3]	2016	cGNSS-R	L1 / LHCP	GPS
^{3}Cat-2 [34]	2016	cGNSS-R rGNSS-R iGNSS-R	L1, L2 / LHCP, RHCP	GPS GLONASS Galileo BeiDou
SMAP GNSS-R [35]	2017	cGNSS-R	L2 / H, V	GPS
BuFeng-1 A/B [36]	2019	cGNSS-R	L1 / LHCP	GPS BeiDou
Spire series [37]	2019	cGNSS-R	L1 / LHCP	GPS Galileo
Fengyun-3 series [38]	2020	cGNSS-R	L1 / LHCP	GPS Galileo BeiDou
^{3}Cat-5 A/B (FSSCat mission) [39]	2020	cGNSS-R	L1 / LHCP	GPS Galileo
^{3}Cat-4 [40]	2021	cGNSS-R	L1, L2 / LHCP	GPS Galileo
PRETTY [41]	2022	iGNSS-R	L1 / RHCP	GPS Galileo
TRITON [42]	2022	cGNSS-R	L1/LHCP	GPS

surfaces, the altimetric range as it is obtained from the delay of the peak was first proposed in [57]. In 2002, a new approach was formulated which consists in fitting a theoretical model to the data. The best fit model implicitly indicates the delay location where the specular point lies [58]. In 2010, it was demonstrated that the maximum of the derivative of the waveform's leading edge corresponds to the specular ray-path delay (except for filtering effects of the limited bandwidth) [59]. The DDM multi-look technique was proposed later. It consists in the acquisition of the full DDM as a way to perform multi-look altimetry beyond the typical pulse-limited region [60]. Additionally, improved altimetric techniques based on phase observations have been tested from an aircraft [61,62] and a zeppelin [63]. The results, for low elevation angles up to ~ 30°, show altimetric precisions comparable to Nadir-looking peak-derivative methods over open sea waters. These results have been confirmed from space, both in near-Nadir geometry over smooth sea ice surfaces [64] and grazing-angle geometries over sea ice and ice sheets [65] and over relatively calm seas [66]. All of the above algorithms are based on cGNSS-R. The peak-derivate method has also been applied in 2013 to iGNSS-R [24], and in 2014 to rGNSS-R [27].

Finally, it is worth to comment that in the spaceborne era, the peak-derivative method [67,68], and the phase observations [66] have also been successfully explored using cGNSS-R. An alternative approach similar to the peak-derivative method was proposed in [24]. It consists in assuming that the specular path delay corresponds to the delay at the 75% [24] and 70% [69] of the peak power. In order to achieve the centimetric accuracy required to track the mean sea level and its spatio-temporal variations, related to large-scale circulation, ocean currents and eddies, or El Niño events, one of the challenging errors to be corrected for is the Electro-Magnetic (EM) bias, which in GNSS-R it also exhibits a dependence with the elevation and azimuth angles [70-72]. Additionally, bandwidth has an important impact in the iGNSS-R waveforms [73]. As the bandwidth is reduced, the Auto Correlation Function (ACF) becomes wider, and the waveform shape approximates to the cGNSS-R approach, using the C/A code only. The displacement produced is small for 20 MHz (40 MHz in RF) (around 14 cm approx.). At 10 MHz (20 MHz in RF), the displacement obtained is around 25 cm, which could start to be relevant.

TABLE II. Summary of some available information on some existing GNSS-R receivers. Type of GNSS-R instruments: G (Ground-based), A (Air-borne), S (Space-borne). GPS-IR means GPS Interferometric Reflectometry, which is a dedicated ground-based technique.

ID	HW/ SW	Number RF Ports	Frequency Bands	BB Bandwidth (MHz)	Sampling Rate (MHz)	Output Rate (Hz)	Receiver Technique	GNSS Constellation	Type
GORS-1(2) [43]	HW	2 (4)	L1, L2	-	-	-	cGNSS-R (C/A, L2C)	GPS, Galileo	G, A
TR	SW	2	L1, L2	-	-	-	Raw	GPS	G
BJ	SW	4	L1, L2	18	20	20,000	Raw	GPS	G
TriG (extended)	HW	8 (16)	Any 4 within L-band	2 to 40 config.	20/40	0.1-1000	Any: software config.	GPS, GLONASS Galileo	G
OceanPal/ SAM	SW	2	L1	4	16.367	1000	Raw	GPS	G
OpenGPS [44]	HW	2	L1	-	5.7	<1000	cGNSS-R (C/A)	GPS	G
COMNAC	SW	1	L1	-	5.7	-	Raw	GPS	G
Ublox LEA-4T	HW	1	L1	2	4	-	cGNSS-R (C/A)	GPS	**G**
NordNav	SW	1(4)	L1	2	16.4	-	Raw	GPS	G
GRAS	HW	3	L1, L2	20	28.25	1000	cGNSS-R (C/A)	GPS	G
DMR [45]	HW	4	L1, L2	4	16	variable	cGNSS-R, raw	GPS	S
NGRx [46]	HW	20	L1, L5	32	65	variable	cGNSS_R, raw	GPS, Galileo, other	S
POLITO-GNSS-R	SW	1	L1	-	8.1838	-	Raw	GPS	G
GRIP-SAR GO	HW	2	L1, L5, E1, E5	52	<=150	1	cGNSS-R	GPS Galileo	G
GLORI [47]	SW	4	L1	4	16.4	-	cGNSS-R	GPS	A
GOLD-RTR [48]	HW	3	L1	8	20	1000	cGNSS-R (C/A)	GPS	G, A
PIR/A [49]	HW	3	L1	12	80	1000	iGNSS-R	Any at L1	G, A
SPIR [50]	SW	16	L1, L5	80	40	40000	Raw	Any at L1, L5	G, A
SPIR--UAV	SW	8	L1, L5	80	40	40000	Raw	Any at L1, L5	A
DODEREC [51,52]	HW	3	L1	-	20.46	-	cGNSS-R (C/A)	GPS	G
SMIGOL [53]	HW	1	L1	2.2	5.745	1	GPS-IR (C/A)	GPS	G
PYCARO [27,54]	SW	2	L1, L2	20	> 100 MHz	Tc and Ti config.	cGNSS-R, rGNSS-R iGNSS-R	GPS, GLONASS, Galileo, BeiDou	G, A, S
PYCARO-2	SW	2	L1, L2, L5 B1, B2, B3 E1, E5	50	> 100 MHz	1	cGNSS-R, rGNSS-R	GPS, GLONASS, Galileo, BeiDou	G
MIR [26]	HW/ SW	2	L1, L5	24	32.736 (x2)	Tc and Ti config.	Raw	GPS Galileo	G, A
FMPL-1 [40]	HW/ SW	2	L1, L2	2	4.096	Tc and Ti config.	cGNSS-R	GPS	S
FMPL-2 [55]	HW/ SW	2	L1, E1	2.4	4.096	Tc = 1 or 4 ms; Ti config	cGNSS-R	GPS L1 C/A Galileo E1	S
FMPL-3	HW/ SW	2	L5 E5a	24	10.230	Tc and Ti config	cGNSS-R	GPS L5 Galileo E5a	S
GENESIS	HW	16	All L-band	-	2 – 40 I/Q config.	1000	cGNSS-R, GNSS-RO, GNSS-PRO	All GNSS and SBAS, >=2 freq. each	A, S

This article has been accepted for publication in a future issue of this journal, but has not been fully edited. Content may change prior to final publication. Citation information: DOI 10.1109/ACCESS.2021.3089762, IEEE Access

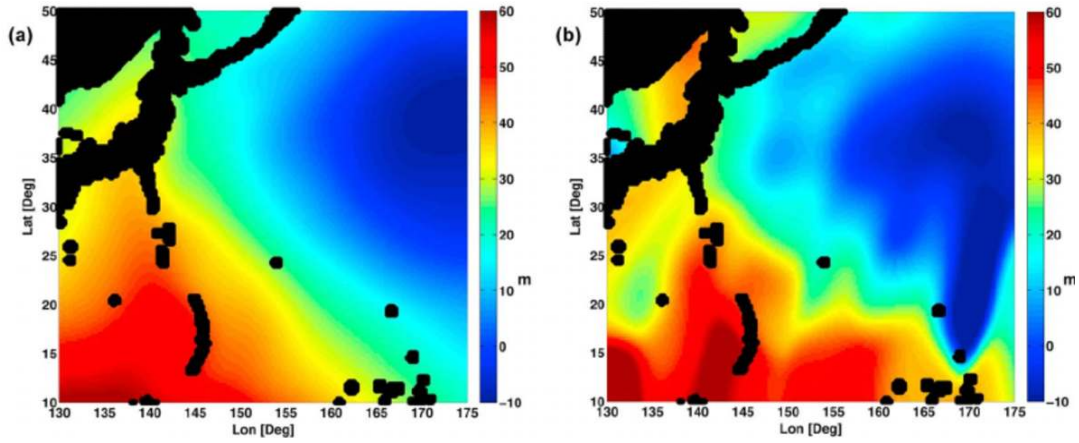

FIGURE 8. **(a) Image of [67]: Technical University of Denmark (DTU) 10 Mean Sea Surface Height (MSSH) over the North Pacific, (b) UK TDS-1 derived MSSH.**

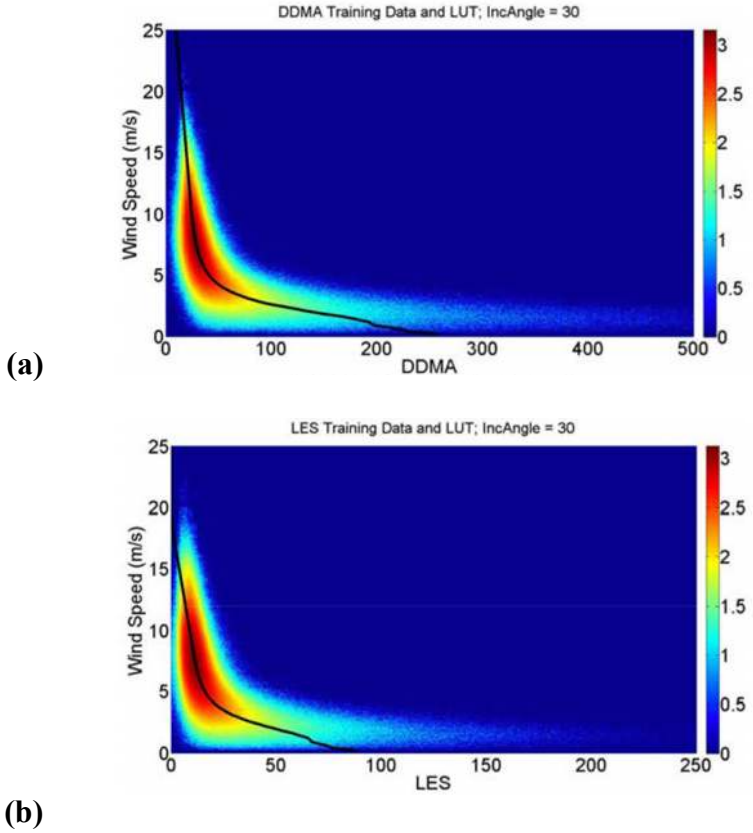

FIGURE 9. **Empirical Geophysical Model Functions (GMFs) for the two Level 1 observables: (a) Delay Doppler Map Average DDMA, and (b) Leading Edge Slope LES, at an incidence angle of ~ 30°, overlaid on log (density) scatter plots of the training data from which they were derived [95].**

2) WIND SPEED

The first wind speed retrieval algorithms were based on the so-called DDM-fit method [74-76]. After re-normalizing and re-aligning the delay-waveform, the best fit against a theoretical model gives the best estimate for the geophysical and instrumental-correction parameters.

Depending on the model used for the fit, the geophysical parameters can be 10-meter altitude wind speed, or sea surface slopes' variance (Mean Square Slopes MSS). Alternative methods perform the fit on the DDM [77,78]. In this way, anisotropic information can be obtained from a single satellite observation. In the so-called trailing-edge methods, the fit is performed on the slope of the trailing-edge [75,79]. Additionally, a stochastic method has been

proposed [80]. It consists of two algorithms to relate the sea roughness conditions with the Doppler spread and the delay spread of the reflected signals. This technique was applied to LEO-based GNSS-R data from the UK-DMC mission [81], where five GNSS-R measured Doppler spreads correlated with the MSS records taken by nearby buoys.

In 2008, simulations indicated that the volume under the normalized DDM or the area under the normalized waveform up to a predetermined threshold are due to the changes in the surface roughness, signals which in turn are also captured in the brightness temperature of the ocean L-band emission [82-84]. Simultaneously, the discrete-Probability Density Function (PDF) method was also proposed [85]. When the bistatic radar equation for GNSS signals is re-organized in a series of terms, each one depending on the surface's slope, the system is linear with respect to the PDF of the slopes. Discrete values of the PDF are therefore obtained. This retrieval does not require an analytical model for the PDF (no particular statistics assumed). When the technique is applied on DDMs, it is possible to obtain the directional roughness, together with others non-Gaussian features of the PDF (such as up/down-wind separation). In 2011 the Normalized Radar Cross Section (NRCS) inversion method was formulated [86]. Numerically efficient methods were presented [86,87] for inverting DDMs to produce a 2-D mapping of the NRCS over the glistening zone [86,87]. All of the above algorithms are based on cGNSS-R.

A feasibility study of wind speed retrieval from space was performed using data from the UK TDS-1 mission [88]. The most successful example of GNSS-R mission for wind speed retrieval is the CYGNSS mission [3], designed primarily for the purpose of monitoring tropical cyclones [89-92], but collecting data over all of the oceans and providing global retrievals of wind speeds [93-95]. These retrievals are achieved using the so-called baseline approach, that implements the minimum variance combination of wind estimates from two observables derived from CYGNSS DDMs, which are known as Delay Doppler Map Average (DDMA) and Leading-Edge Slope (LES) [93-95]. Wind speed estimates derived from each of these observables are obtained via the development of Geophysical Model Functions (GMFs), which consist of 2-D lookup tables of retrieved wind speed, as a function of the observable and the incidence angle (Fig. 9) [95]. The baseline winds provide good quality global wind estimates which have been shown to meet the mission requirements [96], but suffer from significant retrieval biases, especially at high wind speeds [97]. More recently, a retrieval algorithm based on the use of an Artificial Neural Network (ANN) has been also proposed for wind speed estimations from CYGNSS [98].

3) SWELL

At present, there are few studies on the impact of swell on GNSS-R. However, the scattering at L-band can be significantly affected by swell. In 2012, the superposition of the wave spectrum with the swell was evaluated in [99]. In 2013, an air-borne experiment suggested the possibility to measure sea waves periods and heights [100]. That evidence triggered the need to better understand the scattering mechanisms, and to that end, an experiment was performed over a wave channel, showing the feasibility to perform sea waves determination using coherently reflected GPS signals [101]. Simultaneously, the effects of swell on the EM bias were evaluated as a function of the elevation angle [72]. In 2016, the existence of swell effects in low wind speed conditions were analyzed with UK TDS-1 data [102]. In 2020, an analysis in three domains (statistical, time, and spectrum) using air-borne data [103,104] showed the possibility to retrieve wind-driven waves period and swell period thanks to the identification of the secondary peaks [6] present on the coherent component, and other derived products such as the sea state, and the sea surface height with improved resolution. Finally, simulation studies with effects of swell have been compared with TDS-1 data, showing that swell changes the sea surface roughness and has a significant impact on the scattering of GNSS-R signals [105].

3) TARGET DETECTION

GNSS-R constellations could revolutionize sea target detection thanks to the improved spatio-temporal sampling properties [106-110]. In [106], airborne experimental data demonstrated the possibility of ship detection. In [107], the use of DDMs acquired in a backscattered configuration was proposed. The feasibility of sea target detection from a spaceborne platform was showed in [108] using a spatial filter based on steerable antenna beams to solve for the mapping ambiguity. [109] presented a Constant False Alarm Rate (CFAR) method for ship object detection. In [110], a sea target detection algorithm with a spaceborne application was described. It was based on a sea clutter compensation step, using an adaptive threshold to consider spatial variability in the sea background and/or noise statistics. More recently, a few more works [111,112] have provided new insights. In [111], a matched filter was proposed using data from the UK-TDS-1 to detect sea-targets in a DDM sequence without requirements for any (pre)detection. Finally, simulations for ship detection applications at low incidence angle were performed in [112] using a stochastic simulator for sea surfaces.

B. LAND

The use of different GNSS-R techniques for land-surface applications requires further research activities because the dielectric properties of this scattering medium make it more complex than the ocean surface.

1) SOIL MOISTURE CONTENT

The first study on the potential use of GNSS-R for SMC estimation was published in 2000 [113]. Follow-on activities were proposed simultaneously to investigate the

This article has been accepted for publication in a future issue of this journal, but has not been fully edited. Content may change prior to final publication. Citation information: DOI 10.1109/ACCESS.2021.3089762, IEEE Access

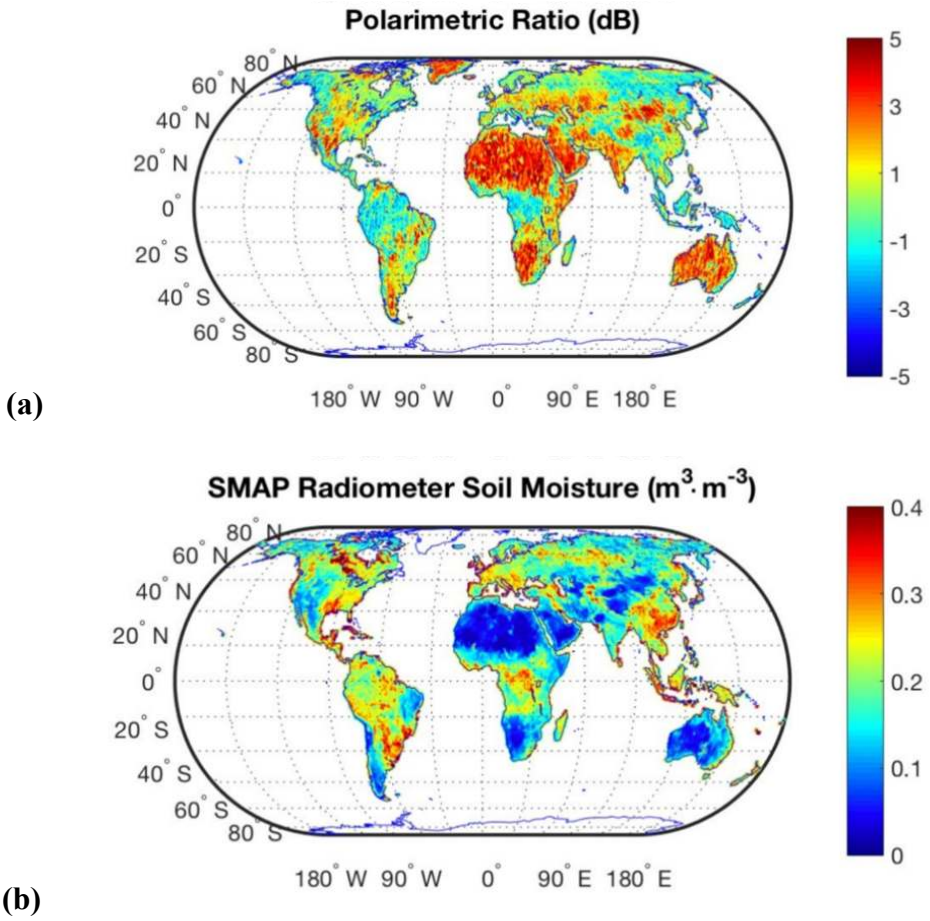

FIGURE 10. **SMAP over-land power waveform analysis using one-year averaged values [35]: (a) Polarimetric ratio, (b) global distribution of time-averaged retrieved surface soil moisture based on SMAP radiometer observations and application of the multi-temporal dual-channel algorithm [125].**

capabilities of GNSS-R for SMC determination using cGNSS-R [114-116] and GPS Interferometric Reflectometry (GPS-IR) [53,117-119]. The use of the polarimetric ratio (ratio of the reflected signals' power at two different polarizations) on cGNSS-R data collected from two airborne experiments was further studied for SMC determination because it can cancel out surface roughness effects [35,120]. A GNSS dual-polarization payload [27] was successfully tested during two experiments from a stratospheric balloon [6]. A comprehensive study over different land surface types was performed to further assess the use of dual-polarization information obtained during two air-borne campaigns [121].

More recently, new important conclusions were also derived. The use of the GPS-IR for accurate SMC estimation was validated over multiple GPS test sites including vegetated surfaces [118,122]. A sensitivity to SMC of ~ 38 dB/(m^3/m^3) was measured over nearly bare-soil target areas using data from UK TDS-1 [123,124]. A Pearson correlation coefficient of r ~ −0.6 between 1 year averaged polarimetric ratio from a GNSS-R experiment on-board the Soil Moisture Active Passive (SMAP) mission and SMC (Fig.10) was measured over the complete Earth's surface [35,125]. The elevation angle should be considered for the application of the so-called Tau-Omega model in the GNSS-R case [9]. Daily averaged CYGNSS-derived and SMAP-derived SMC showed a good agreement over specific test sites [126]. A better sensitivity of CYGNSS to SMC appeared over croplands when the coherent scattering term became dominant over the incoherent one, with a sensitivity to SMC of ~ 50 dB/(m^3/m^3) [127]. It was found that the ratio of the coherent-to-incoherent scattering terms depends on the elevation angle [127,128]. The reflectivity was found to be a better SMC estimator than the SNR. Additionally, it was found a significant influence of the elevation angles on the results [128].

Several works have demonstrated the possibility to estimate SMC using CYGNSS data. A retrieval approach based on incoherent scattering was presented in [129], under the assumption that vegetation and roughness

This article has been accepted for publication in a future issue of this journal, but has not been fully edited. Content may change prior to final publication. Citation information: DOI 10.1109/ACCESS.2021.3089762, IEEE Access

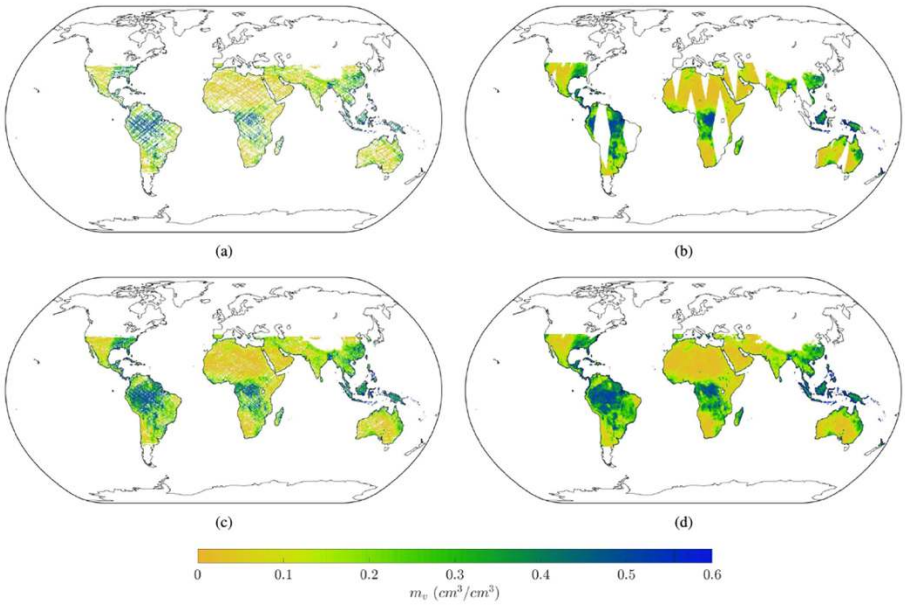

FIGURE 11. Comparisons of SMAP and CYGNSS SMC [129] on time scales of 1 day and 3 days on a 0.2° × 0.2° latitude/longitude grid. (a) Retrieved SMC using CYGNSS land returns over 1 day, (b) SMAP SMC over 1 day, (c) retrieved SMC using CYGNSS land returns over 3 days, (d) SMAP SMC over 3 days.

changes occur on timescales longer than those associated with soil moisture changes. Results suggested that global SMC retrieval with an RMS error on the order of ~ 0.04 cm^3/cm^3 is possible over varied terrain (Fig. 11). Simultaneously, the so-called Reflectivity-Vegetation-Roughness R-V-R algorithm was implemented in [130]. The CYGNSS-derived SMC values that were estimated globally agreed well with SMAP collocated measurements, delivering an overall RMS error of ~ 0.07 cm^3/cm^3. The University Corporation for Atmospheric Research (UCAR) / University of Colorado (CU) SMC product was presented in [131]. This product was derived using the empirical relationships between the reflectivity and SMAP-derived SMC. It was validated at 171 in-situ soil moisture stations, which resulted in a median unbiased RMSE of ~ 0.049 cm^3/cm^3. At present, the main remaining challenges are to properly correct for the impact of the upwelling vegetation cover and the small-scale surface roughness in the reflectivity, so as to improve the accuracy in SMC retrievals [132]. To do so, multi-pass and single-pass techniques can be applied, each one with pros and cons. Finally, it worth to mention that a significant effort has been performed in the development of simulation tools to better understand SMC retrieval capabilities from a space-borne platform [133].

2) BIOMASS

Some pioneering studies showed a promising sensitivity to forest biomass. Scattering simulations based on the Bistatic MIchigan MIcrowave Canopy Scattering (Bi-MIMICS) model at linear polarization (Horizontal H, Vertical V) suggested a better sensitivity than monostatic configurations for canopy Height CH ~ 8 m [134]. This result was consolidated using the Tor Vergata model at circular polarization (RHCP, LHCP) for higher levels of biomass up to AGB ~ 200 ton/ha [135]. Direct and multiple scattering terms were evaluated using Bi-MIMICS [136] at circular polarization (RHCP, LHCP). It was concluded that the total scattering field at both polarizations RHCP and LHCP is dominated by the scattering over the tree trunks layer. The Soil and Vegetation Reflection Simulator (SAVERS) was developed using the Tor Vergata electromagnetic model [135]. SAVERS includes capabilities to predict signal power as measured by a GNSS-R reflectometer, considering system properties, and observation geometry [116]. Two airborne experiments confirmed the sensitivity of the bistatic reflectivity up to high levels of AGB ~ 300 ton/ha [137].

Empirical results over boreal forests from a stratospheric balloon suggested that the coherent scattering term is roughly independent of the platform's height [138]. The EMISVEG [139] and the Signals of opportunity Coherent Bistatic scattering model for Vegetated terrains (SCoBi-Veg) [140] simulators further analyzed this hypothesis. Lindenmayer systems [141] were used to generate fractal geometry and the Foldy's approximation [142] was used to account for attenuation and phase change of the coherent wave propagating in the forest media. More recently, a comprehensive study [143] demonstrated a significant sensitivity of several GNSS-R observables up to

This article has been accepted for publication in a future issue of this journal, but has not been fully edited. Content may change prior to final publication. Citation information: DOI 10.1109/ACCESS.2021.3089762, IEEE Access

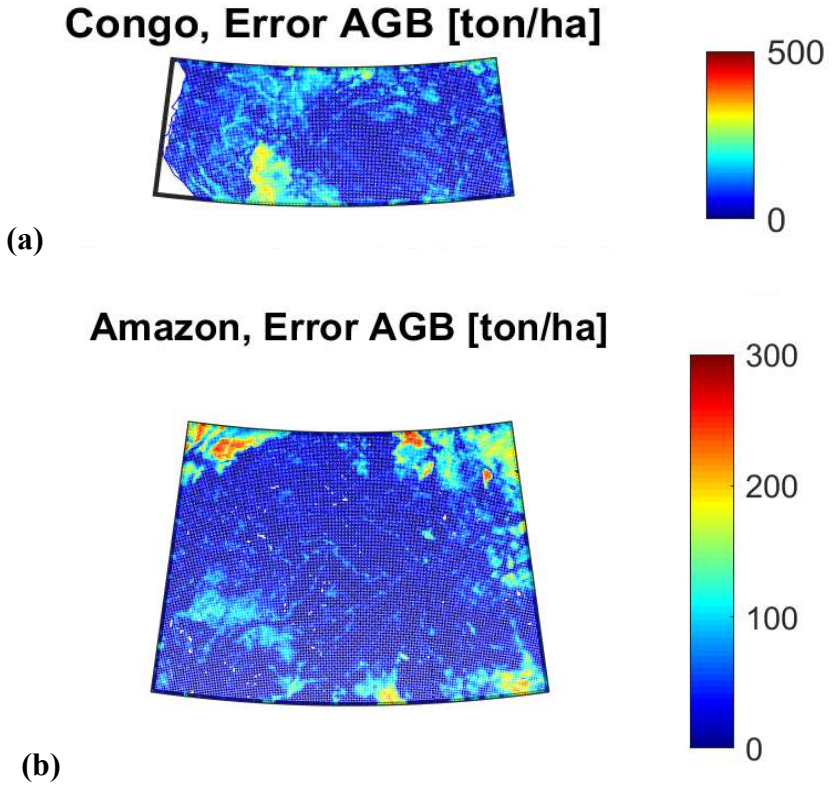

FIGURE 12. **Absolute error in AGB retrieval over (a) Congo, and (b) Amazon [144]. Trailing edge was used at grazing angles. Empirically derived polynomial fitting functions were used.**

AGB ~ 150 ton/ha at different elevation angles using the GLObal navigation satellite system Reflectometry Instrument (GLORI) instrument [47]. Feasibility studies for the case of GNSS-R data collected from a spaceborne platform have shown a certain sensitivity to forests biomass on a global scale using the SMAP radar receiver [35]. CH was demonstrated to be a key parameter, with a higher impact in GNSS-R signatures than Normalized Difference Vegetation Index (NDVI). More recently, the first maps of absolute error in AGB retrieval from space using GNSS-R were generated, showing a small error over areas with an AGB up to ~ 500 ton/ha (Fig. 12). These findings suggest the possibility of accurate AGB retrieval using GNSS-R on-board small satellites such as, e.g., CYGNSS [144]. Additionally, experimental results have suggested that for beech forest, NDVI is a good descriptor of signal attenuation at L-band, which is known to be related to the Vegetation Optical Depth (VOD) [145]. Depolarization effects were also studied and they were found to be significant at elevation angles as large as ~ 50° [145].

3) INLAND WATER BODIES

GNSS-R data have also been exploited for inland water monitoring thanks to the enhanced spatial resolution and increased reflected power under the coherent scattering regime [146-149]. GNSS-R airborne data collected over the Ebro River Delta (Spain) and spaceborne data over the Mississippi River (USA) demonstrated that inundated wetlands can be identified under different vegetation conditions [146]. Later, [147] showed that CYGNSS data provide clear evidence of surface saturation and inundation extent over land with higher spatio-temporal sampling than more traditional microwave radiometers such as e.g. SMAP. [148] showed that CYGNSS watermasks provide accurate, time-varying maps that are able to resolve changes in lake and river position and extent. [149] demonstrated that CYGNSS has a capability for frequent, high-resolution observations of wetland dynamics across a wide range of timescales in the tropics. Finally, [150] demonstrated the creation of dynamic inland water body masks at spatial resolutions ranging from 1 to 3 km through the use of a recently developed coherence detector for the delay-Doppler maps produced by the CYGNSS constellation.

This article has been accepted for publication in a future issue of this journal, but has not been fully edited. Content may change prior to final publication. Citation information: DOI 10.1109/ACCESS.2021.3089762, IEEE Access

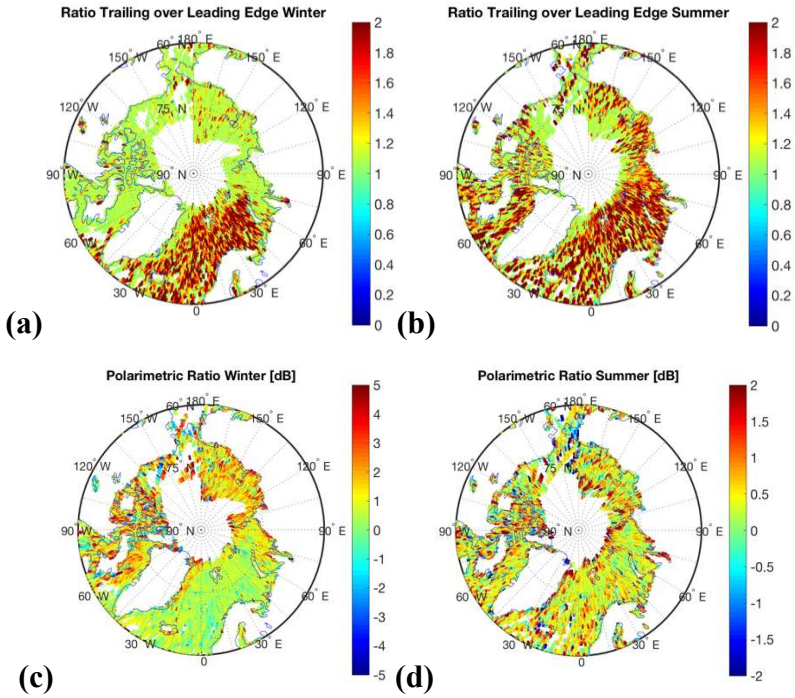

FIGURE 13. **Ratio of the trailing over the leading edge [164]: (a) Winter, (b) Summer. Polarimetric Ratio [164]: (c) Winter, (d) Summer.**

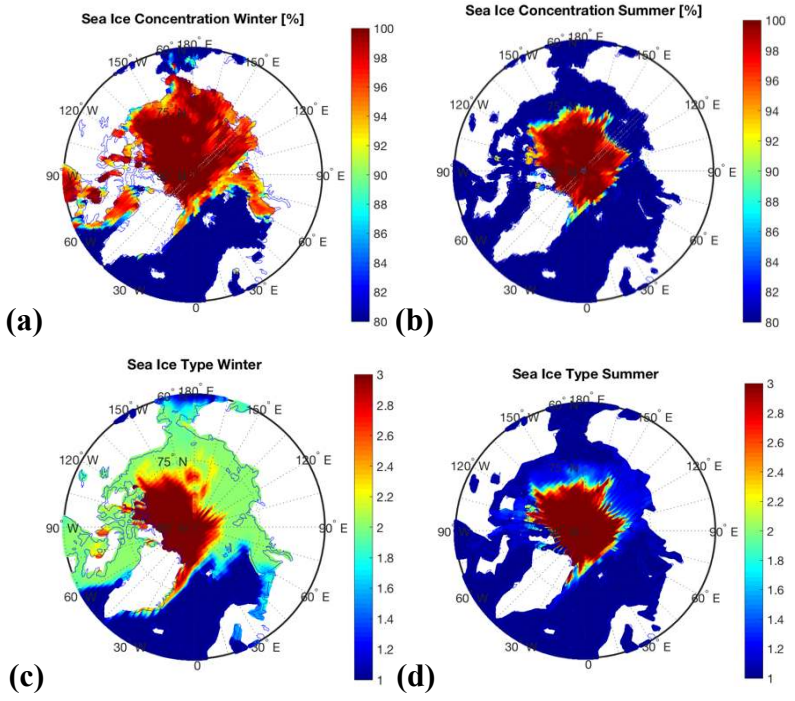

FIGURE 14. **Sea ice concentration: (a) Winter, (b) Summer. Sea ice type: (c) Winter, (d) Summer. Data provided by the European Organisation for the Exploitation of Meteorological Satellites (EUMETSAT) Ocean and Sea Ice Satellite Application Facility (OSISAF). (1) no ice or vey open ice; (2) relatively young ice; (3) ice that survived a summer melt. Probability of miss-detection filtered out in data processing.**

C. CRYOSPHERE

At present, there is also an increasing number of GNSS-R applications in the cryosphere.

1) SNOW

The first study on GNSS-R over thick dry snow masses was the theoretical investigation performed in [151]. Later, the GPS-IR technique was used in several experiments,

This article has been accepted for publication in a future issue of this journal, but has not been fully edited. Content may change prior to final publication. Citation information: DOI 10.1109/ACCESS.2021.3089762, IEEE Access

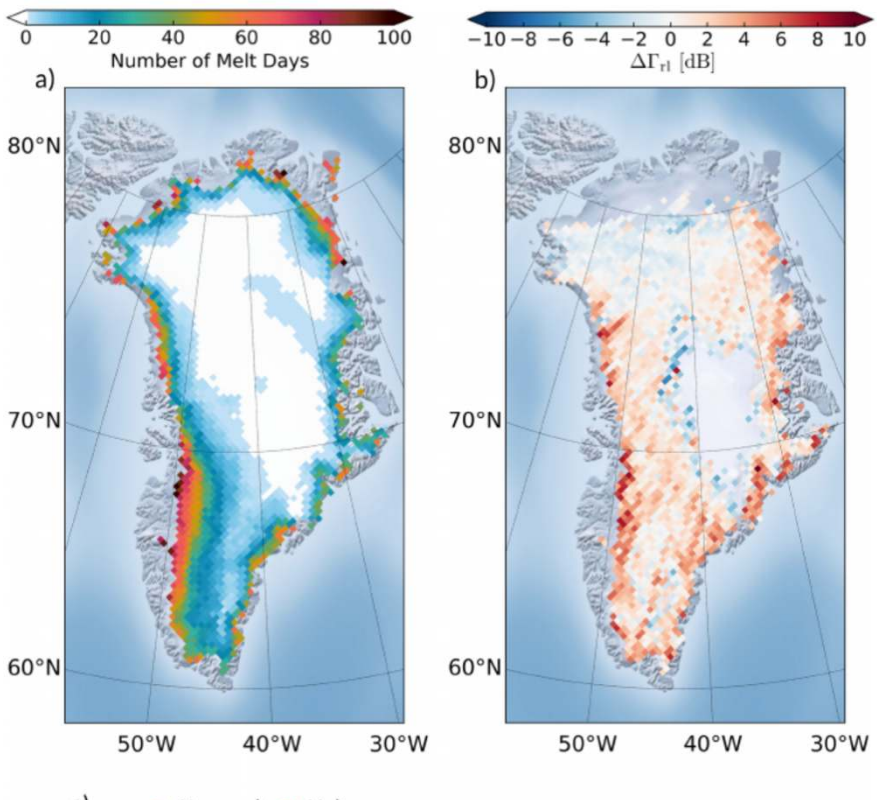

FIGURE 15. (a) The number of melt days over the Greenland ice sheet for each 25-km grid cell, which is accumulated from the Greenland daily microwave radiometer surface melt map during the 2018 melt season (May–October), and (b) the averaged changes in GNSS-R reflectivity for each grid cell computed with the UK TDS-1 data collected during the 2018 melt season (May–October) [174].

including the use of frequency [152], and frequency and amplitude [153] measurements. In 2011, the use of the GPS-IR at linear [154] and circular [155] polarization was explored. Alternatively, radio-holographic techniques were used on each lag of the delay-waveform to identify the spectral content of the signal, and to identify each frequency-component to different snow depths, reaching down to ~ 300 meters depth in polar ice sheets of the Antarctica [156].

2) SEA ICE

In 2011, phase-delay observations [155-157] were used to monitor the tidal signatures of floating sea ice in Greenland. Alternatively, the peak-power method was used to estimate the permittivity [158]. An empirical model was generated after comparison of the peak power of GPS reflections received by air-borne instruments with RADARSAT backscattered peak power. This method was also applied to spaceborne UK-DMC data and compared to Sea Ice Concentration (SIC) measurements obtained with the Advanced Microwave Scanning Radiometer-E (AMSR-E) and ice charts [159]. However, this observable can be strongly affected by the sea ice surface roughness. To overcome this limitation, the polarimetric ratio was explored in [160]. Linear [161] and circular [162] polarimetric phase shift methodologies were used as a means to estimate the permittivity. A different approach to obtain the sea ice roughness by fitting the waveform shape was used in [162,163]. This method showed potential for characterization of the different stages of sea ice after the comparison with other remote sensing techniques. In 2013, the scatterometric fit method [156] was used to estimate sea ice roughness. In 2011, a certain correlation was found [155,156] between the coherence time of the reflected signals and the wind over the zone. All of the above algorithms are based on cGNSS-R.

In the spaceborne era, a GNSS-R study was performed over the Artic from SMAP in 2017 [35,164,165]. The sensitivity of several observables (SNR, polarimetric ratio, ratio of the trailing- over the leading- edge, and slope of the trailing-edge) to seasonal fluctuations of SIC was evaluated. The use of the polarimetric ratio at linear polarization was found to provide improved results (Figs. 13,14). This observable followed the Fresnel reflection coefficients for a smooth surface (sea ice): > 2 dB (Winter) vs. ~ 0.5 dB (Summer). Additionally, several spaceborne experiments have been performed from the UK TDS-1. In 2017, a sea ice detection algorithm was developed using data over the Arctic and the Antarctic regions based on the

similarity of the received GNSS reflected waveform to the coherent reflection model waveform [166].

In 2018, the use of Convolutional Neural Networks (CNNs) was proposed for sea ice detection and SIC prediction [167]. In 2019, a framework that employs Support Vector Machines (SVMs) was proposed for the classification of DDMs, specifically, for separating DDMs of sea ice from those of sea water [168]. The developed approach shows improved sea ice detection performance with respect to the existing NN- and CNN-based algorithms in terms of, first, enhanced accuracy and improved robustness with respect to false alarm, second, less DDM data storage requirements, and finally, fewer tuning parameters [169]. In 2020, an effective schematic was developed for estimating Sea Ice Thickness (SIT) from the reflectivity, which was formulated as the product of the propagation loss due to SIT and the reflection coefficient of underlying sea water [170]. A GMF for SIC retrieval has been also developed based on a new observable termed as differential delay waveform (DDW) [171]. Finally, the potential of GNSS-R to classify ice types during the sea ice formation period was demonstrated using a sea ice multi-step classification approach based on UK TDS-1 data and Synthetic Aperture Radar SAR-derived sea ice type maps [172].

3) GLACIERS

A GNSS-R experiment over Greenland ice sheet was performed from SMAP in 2017 [35] using several observables (SNR, polarimetric ratio, and trailing-edge). Two main conclusions were found: a) It is feasible to monitor melting on the ice sheet and the corresponding seasonal fluctuations, b) the spreading of the waveforms increases with the amount of dry ice because of the impact of the volume scattering term. Over dry ice, volume scattering and scattering at different layers could occur allowing the GNSS signals to penetrate the subsurface. These findings triggered the possibility of cryosphere monitoring using GNSS-R sensors from space. Several dedicated studies over Greenland have also been performed with data provided by the UK TDS-1 mission. In [173], the information contained in the DDMs were inverted to obtain altimetric estimates, and the retrieved height showed, as expected, significant discrepancy with the ice surface elevation corresponding to the topography given by National Snow and Ice Data Center (NSIDC) Geoscience Laser Altimeter System (GLAS) data from the Ice, Cloud, and land Elevation Satellite (ICESat-1). The difference between the GNSS-R derived surface height and the ice surface elevation was attributed to the penetration of the L-band signal into the ice-sheet. In 2020, ice-sheet melting occurrence was detected using the reflectivity increment from the empirical background reflectivity (Fig. 15) [174].

V. GNSS+R 2021 AND BEYOND

Continuing the series of GRSS-co-sponsored conferences, GNSS+R 2021 will be held in Beijing, China. GNSS+R 2021 will be an international forum for reporting and discussing recent achievements in GNSS-R and other signals of opportunity. The meeting will focus on the latest advances in GNSS-R theory and modeling, instrumentation, algorithms and applications in the field of ocean, land, and cryosphere remote sensing. The “Standard for Spaceborne GNSS-R Data and Metadata Content” working group will meet there to share our standard [11] with all the potential users in the community.

VI. SUMMARY AND OUTLOOK

Future advancements on satellite subsystems and retrieval algorithms will further explore the performance of GNSS-R to derive geophysical parameters of interest such as wind speed, ocean surface height, soil moisture content, biomass, inland water, and sea ice. As such, the GNSS-R standard is focused on the definition of the L1 parameters required for the generation of scientifically valuable products. We aim to provide a strong foundation for GNSS-R data to further explore and shift the limits of this technique, independently of constraints imposed by current limitations on geophysical parameters retrieval algorithms. In this article, an overview of the different GNSS-R techniques with a spaceborne application has been shown. Additionally, a description of the most common retrieval algorithms has demonstrated the wide range of scientific applications of GNSS-R over ocean, land, and cryosphere. On the other hand, we have compiled some available information on most of the existing GNSS-R receivers. The wide variety of techniques, algorithms, and instruments motivated the development of this working group.

The GNSS-R community has been growing rapidly during recent years. In the next decade, constellations of small satellites (Fig. 16) are expected to be launched into space, and works have also proposed larger missions [20-22] (Fig. 17). As such, we should plan future data sets so that valuable and inter-comparable products will result with a view to enable long-term stability and retrieval consistency in support of science and operational applications.

VII. ON-LINE RESOURCES

GNSS+R Bibliography, Institute of Space Sciences. Online available: https://www.ice.csic.es/personal/rius/gnss_r_bibliography/index.html

Cyclone Global Navigation Satellite System, University of Michigan. Online available https://clasp-research.engin.umich.edu/missions/cygnss/ (07/07/2020).

PEPS/GEROS GNSS-R Simulator, Universitat Politecnica de Catalunya. Online available:

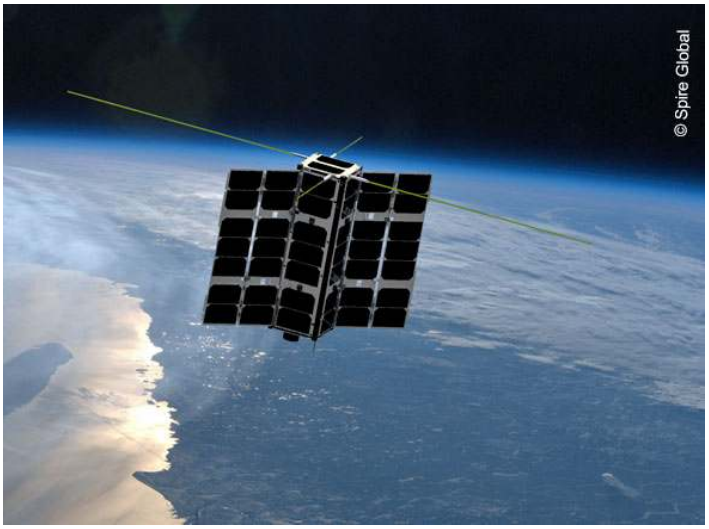

FIGURE 16. **Artist's view of a Spire GNSS-R CubeSat mission. Image credits Spire Global.**

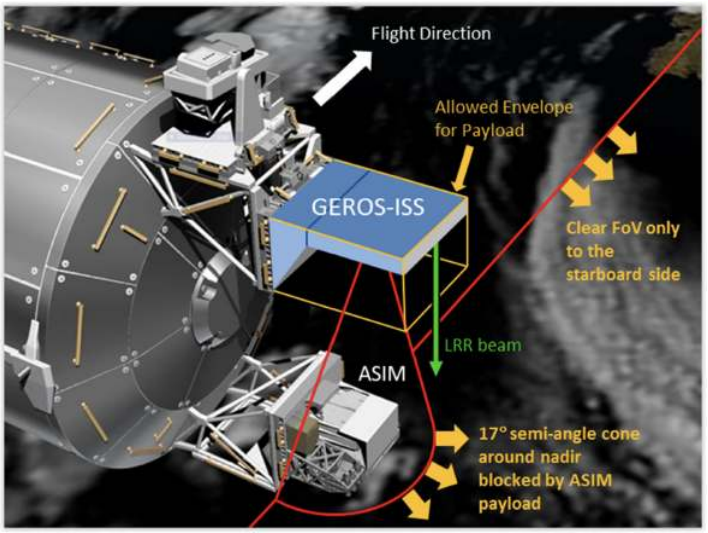

FIGURE 17. **Artist's view of GEROS deployment at the upper Columbus External Payload Facility "upper balcony" of the ISS Columbus module with limited field of view [20].**

https://prs.upc.edu/2018/07/19/gnss-r-simulator/ (07/07/2020).
GEROS-SIM4LAND GNSS-R Simulator, Universitat Politecnica de Catalunya. Online available: http://147.83.91.189/ (07/07/2020).
P4003 - Standard for Global Navigation Satellite System-Reflectometry (GNSS-R) Data and Metadata Content, IEEE GRSS. Online available: https://standards.ieee.org/project/4003.html (07/07/2020).

APPENDIX: THE GNSS CONSTELLATIONS

An overview of the 4 GNSS constellations (Table A1) is provided in this Appendix. Understanding the heterogeneous nature of these signals of opportunity as well as the numerous types of constellations is important in the GNSS-R scenario.

A. GPS

GPS is a robust constellation consisting of 31 operational SVs plus 5 spares. More decommissioned satellites are in orbit and available as spares. Satellites are distributed over six orbital planes, separated by a Right Ascension of the Ascending Node (RAAN) of ~ 60°, with an orbital inclination of ~ 55°, and with an orbital radius of ~ 26,600 km. Each satellite orbits the Earth twice every sidereal day, and the same ground track is repeated once per day. Therefore, the same constellation geometry can be observed every day with ~ 4 minutes (235.909 seconds) difference. At the time of writing this article the constellation is

This article has been accepted for publication in a future issue of this journal, but has not been fully edited. Content may change prior to final publication. Citation information: DOI 10.1109/ACCESS.2021.3089762, IEEE Access

TABLE A1. Parameters of the most common GNSS signals used in GNSS-R: GPS L1 C/A, GPS L2 P(Y), GPS L2 C, Galileo E1 OS, GLONASS C/A L1 and L2, GLONASS L2 P, and BeiDou B3I.

GNSS system	GPS	GPS	GPS	GPS	Galileo	GLONASS	GLONASS	GLONASS	BeiDou
Code name	C/A	P(Y)	CM	CL	E1 OS	C/A	C/A	P	B3I
Center Frequency (MHz)	1575.42	1227.6	1227.6	1227.6	1575.42	(1598.0625-1605.375) ± 0.511	(1242.93-1248.625) ± 0.511	(1242.93-1248.625 ± 0.511	1268.52
Frequency band	L1	L2	L2	L2	E1	L1	L2	L2	L2
Access technique	CDMA	CDMA	CDMA	CDMA	CDMA	FDMA	FDMA	FDMA	CDMA
Modulation	BPSK (1)	BPSK (10)	BPSK (1) results of multiplexing two streams of 511.5 kHz	BPSK (1) results of multiplexing two streams of 511.5 kHz	CBOC (6,1,1/11)	BPSK (0.511)	BPSK (0.511)	BPSK (0.511)	BPKS (10)
Sub-carrier frequency (MHz)	-	-	-	-	1.023 and 6.138 (Two sub-carriers)	-	-	-	-
Chipping rate (MHz)	1.023	10.23	0.5115	0.5115	1.023	0.511	0.511	0.511	10.23
Signal component	Data	Data	Data	Pilot	Data Pilot	Data	Data	Data	Data
Primary PRN code length	1023	6.19 x 1012	10230	767250	4092	511	511	-	10230
Code Family	Gold codes	Combination and short cycling of M sequences	M-sequence from a maximal polynomial of degree 27	M-sequence from a maximal polynomial of degree 27	Random Codes	M-sequences	M-sequences	-	-
Secondary PRN code length	-	-	-	-	25	-	-	-	-
Data rate	50 bps	50 bps	IIF 50 bps; IIR-M also 25 bps	NA	250 bps NA	50 bps	50 bps	250 bps	50
Minimum received power (dBW)	-158.5	II/IIA/IIR -164.5 IIR-M -161.4 IIF -160.0	II/IIA/IIR -164.5 IIR-M -161.5 IIF -161.5	-157	-157	-161	-167	-	-163

composed of the following satellites: 9 GPS IIR transmitting the L1 C/A, L1 P(Y), and L2 P(Y) signals, 7 GPS IIRM transmitting the L1 C/A, L1 P(Y), L2 P(Y), L2C, L1M, and L2M signals, 12 GPS IIF transmitting the L1 C/A, L1 P(Y), L2 P(Y), L2C, L1M, L2M, and L5 signals, and 3 GPS IIIA transmitting the L1 C/A, L2 P(Y), L2C, L1M, L2M, and L5 signals. The GPS III satellites provide four civil signals, and they use 3 improved Rubidium atomic clocks. The GPS ground segment is composed by a primary master control station at Schriever Air Force Base (Colorado, USA), and 10 dedicated ground antennas and monitor stations.

B. GLONASSS

GLONASS was created by the Soviet Union and it became fully operational in 1995. Later, the constellation was reduced reaching a minimum of 8 operational satellites in 2002. However, since 2010 it is again fully operational and is currently composed of a total of 29 SVs from which 23 SVs are operational, 1 SV is in commissioning phase, 2 SVs are in maintenance, 1 SV is in flight tests phase, and 1 SV is a spare. GLONASS satellites orbit in three orbital planes inclined ~ 64.8° and separated by ~ 120°. Each plane includes 8 satellites equally spaced by ~ 45°, and the orbital radius is of ~ 25,511 km.

New SVs (GLONASS-K2) will improve the accuracy of current GLONASS-M and broaden the application domain. In particular, it is expected to achieve the following technical advantages: Longer guaranteed lifetime, modernization of SVs' support systems, improvement of

on-board synchronizer stability, advanced technologies for monitoring and control, orbit and clock data provision, additional payloads and new signals (L1 OF, L2 OF, L1 SF, L2 SF, L1 OC, L1 SC, L2 OC, L2 SC, L3 OC). The first GLONASS-K2 launch took place in 2018. They are currently in testing phase. The key features of this new generation of satellites are the following:

• The SVs will allow the accommodation of all on-board specialized equipment without any restrictions.

• The on-board subsystems will provide operational conditions for the specialized instruments without any constraints imposed by power consumption and thermal control.

• The maximum pointing error will be better than ~ 0.25°.

• The Inter-Satellite Link (ISL) will allow continuous operation during one cycle (reception-transmission) without restrictions.

• Additional payloads to perform tests in space environment and to achieve flight qualification could be accommodated.

The GLONASS ground control segment includes the deployment of a measuring station network in Russia and Antarctica, the deployment of an uplink station network in Russia, the deployment of a global measuring station outside Russia, and the further use of crosslink functions for ephemerides and clock data provision.

C. GALILEO

In March 2002, the European Union (EU) and the European Space Agency (ESA) agreed to develop the Galileo navigation system, which was expected to be fully functional by 2020. At the time of writing this document, Galileo is under development, and it will be fully compatible with the modernized GPS system. At present, GNSS receivers are able to combine signals from several constellations to increase significantly the achievable accuracy. As compared to the USA GPS and the Russian GLONASS, Galileo is designed specifically for civilian and commercial purposes. The In-Orbit Validation Element (GIOVE) A and B SVs, dedicated to take the first step of the in-orbit validation phase towards full deployment of Galileo, were launched in 2005 and 2008 respectively, and retired in 2012. Three In-Orbit Validation (IOV) SVs were launched from 2011 to 2012, being fully operational in 2015. At present, the Galileo constellation is composed of 22 operational SVs from which 3 SVs are IOV type, 19 SVs are Full Operational Capability (FOC) type, 2 SVs are in testing phase, 2 SVs are unavailable, and 2 SVs have been retired. The full constellation will consist of 30 SVs, 24 SVs operational and 6 active spares, distributed in three orbital planes (~ 56° inclination) with an orbital radius of ~ 26,600 km and with an orbital period of ~ 14 h.

Technology advances include:

• To improve robustness, quicker recovering from failures, and the Orbit Determination and Time Synchronization (ODTS) system, so as to provide long-term ephemerides. More specifically, improvements are required on Passive Hydrogen Maser (PHM), mini PHM, robust Rubidium Atomic Frequency Standard (RAFS) and cesium clocks.

• Increased SV capability while maintaining as a minimum the same launch cost efficiency (to confirm by testing the capability of state-of-the-art electric propulsion subsystems).

• Enabling either communication and/or ranging capabilities (in-plane and inter-plane ISL, ODTS exploiting ISL ranging, communication capabilities used for navigation message dissemination and for improving system robustness).

• The technology advances related to the improvement of the ODTS system are the following: Use of several faster navigation messages, improvement of orbit modelling, use of advanced navigation messages by means of Signal-In-Space (SIS) spare bits/words, d) enhancing fault detection mechanisms, and e) use of adaptive clock fitting.

D. BEIDOU

BeiDou consists of 2 separate satellite constellations. The first BeiDou system, officially called the BeiDou Satellite Navigation Experimental System (BeiDou-1), consisted of 3 satellites. BeiDou-1 offered limited coverage and navigation services, mainly for users in China and neighboring regions. BeiDou-1 was decommissioned at the end of 2012. The second generation of the system, officially known as COMPASS or BeiDou-2, became operational in China in December 2011, with a partial constellation of 10 satellites in orbit. Since December 2012, it has been offering services to customers in the Asia-Pacific region (currently 15 operational SVs). In 2015, China launched the third generation of the BeiDou system (BeiDou-3) for global coverage. The first BeiDou-3 satellite was launched on March 30th 2015. On December 27th 2018, BeiDou-3 started providing global services, and the final satellite was launched into orbit on June 23th 2020.

BeiDou-3 is composed of a total of 34 SVs, 29 SVs operational, and 5 spares. BeiDou-3 utilizes high stability hydrogen atomic and rubidium clocks. Additionally, ISLs help with time synchronization, and enhance search & rescue services and Message Communication Services (MCS), including regional MCS and global short MCS. The Radio Determination Satellite Service (RDSS) payload of the Beidou-3G satellites consists of a high-power S-band transponder, a low-noise L-band amplifier and frequency generator, a phased array L-band antenna, a L-/S-band dish antenna and a C-band antenna. RDSS uses the original position retrieval including the central ground station to provide compatibility of the new system with existing BeiDou-1 terminals. On the other hand, the Radio Navigation Satellite Service (RNSS) payload uses ultra-stable timing signals delivered by an atomic clock to generate L-band signals that are transmitted through an antenna array. RNSS also includes an L-band uplink

receiver and laser reflector for orbit determination. This payload works on the same principle as GPS and Galileo, using similar frequency bands.

REFERENCES

[1] H. Carreno-Luengo, A. Camps, N. Floury, M. Martin-Neira, C. Ruf, T. Wang, S.-J. Khalsa, M.-P. Clarizia, J. Reynolds, J. Johnson, A. O'Brien, C. Galdi, M. di Bisceglie, A. Dielacher, P. Jales, M. Unwin, L. King, G. Foti, R. Shah, D. Pascual, B. Schreiner, M. Asgarimehr, J. Wickert, S. Ribo, and E. Cardellach, "The GRSS Standard for GNSS-Reflectometry," in Proc. of the 2020 IEEE IGARSS, Hawaii, USA, July 2020.

[2] P. Jales et al. "MERRByS Product Manual – GNSS Reflectometry on TDS-1 with the SGR-ReSI," online available http://merrbys.co.uk/wp-content/uploads/2018/12/0248366_MERRByS-Product-Manual-GNSS Reflectometry-on-TDS-1-with-the-SGR-ReSI-v005.pdf (accessed 1 July 2020)

[3] C. Ruf et al., "CYGNSS Handbook. Cyclone Global Navigation Satellite System," online available https://clasp-research.engin.umich.edu/missions/cygnss/reference/cygnss-mission/CYGNSS_Handbook_April2016.pdf (accessed 20 June 2020)

[4] V.U. Zavorotny, S. Gleason, E. Cardellach, and A. Camps. "Tutorial on Remote Sensing Using GNSS Bistatic Radar of Opportunity", IEEE Geoscience and Remote Sensing Magazine, vol. 2, no. 4, pp. 8-45, 2014.

[5] M. Martin-Neira, "A Passive Reflectometry and Interferometry System (PARIS): Application to Ocean Altimetry," ESA J., vol. 17, no. 4, pp. 331-355, 1993.

[6] H. Carreno-Luengo, A. Camps, J. Querol, and G. Forte, "First Results of a GNSS-R Experiment from a Stratospheric Balloon over Boreal Forests," IEEE Transactions on Geoscience and Remote Sensing, vol. 54, no. 5, pp. 2652–2663, 2015.

[7] A. Alonso-Arroyo, A. Camps, H. Park, D. Pascual, R. Onrubia, and F. Martín, "Retrieval of Significant Wave Height and Mean Sea Surface Level Using the GNSS-R Interference Pattern Technique: Results From a Three-Month Field Campaign," IEEE Transactions on Geoscience and Remote Sensing, vol. 53, no. 6, pp. 3198-3209, 2015.

[8] A.G. Voronovich, and V.U. Zavorotny "Bistatic Radar Equation for Signals of Opportunity Revisited," IEEE Transactions on Geoscience and Remote Sensing, vol. 56, no. 4, pp. 1959-1968, 2018.

[9] H. Carreno-Luengo, G. Luzi, and M. Crosetto, "Sensitivity of CYGNSS Bistatic Reflectivity and SMAP Microwave Radiometry Brightness Temperature to Geophysical Parameters over Land Surfaces," IEEE Journal of Selected Topics in Applied Earth Observations and Remote Sensing, vol. 12, no. 1, pp. 107-122, 2019.

[10] H. Carreno-Luengo, C.Ruf, A. Warnock, and K. Brunner, "Investigating the Impact of Coherent and Incoherent Scattering Terms in GNSS-R Delay Doppler Maps," in Proc. of the 2020 IEEE IGARSS, Hawaii, USA, July 2020.

[11] H. Carreno-Luengo, A. Camps, N. Floury, M. Martin-Neira, C. Ruf, T. Wang, S.J. Khalsa, M.P. Clarizia, J. Reynolds, J. Johnson, A. O'Brien, C. Galdi, M. di Bisceglie, A. Dielacher, P. Jales, M. Unwin, L. King, G. Foti, R. Shah, D. Pascual, B. Schreiner, M. Asgarimehr, J. Wickert, S. Ribo, and E. Cardellach, "IEEE Standard for Global Navigation Satellite System-Reflectometry (GNSS-R) Data and Metadata Content," IEEE Standards Association, (submitted).

[12] M. Semmling, V. Leister, J. Saynisch, F. Zus, S. Heise, and J. Wickert, "A Phase-Altimetric Simulator: Studying the Sensitivity of Earth-Reflected GNSS Signals to Ocean Topography," Transactions on Geoscience and Remote Sensing, vol. 54, no. 11, pp. 6791-6802, 2016.

[13] V.A. Nguyen, O. Nogues-Correig, T. Yuasa, D. Masters, and V. Irisov, "Initial GNSS Phase Altimetry Measurements from the Spire Satellite Constellation," Geophysical Research Letters, vol. 47, no. 15, 2020.

[14] M. Martin-Neira, S. D'Addio, C. Buck, N. Floury, and R. Prieto-Cerdeira, "The PARIS Ocean Altimeter In-Orbit Demonstrator," IEEE Transactions on Geoscience and Remote Sensing, vol. 49, no. 6, pp. 2209-2237, 2011.

[15] J. Garrison, and S.J. Katzberg, "The Application of Reflected GPS Signals to Ocean Remote Sensing," Remote Sensing of the Environment, vol. 73 no. 2, pp. 175-187, 2000.

[16] S. Gleason, C. Ruf, A. O'Brien, and D. MacKague, "The CYGNSS Level 1 Calibration Algorithm and Error Analysis Based on On-Orbit Measurements," IEEE Journal of Selected Topics in Applied Earth Observation and Remote Sensing, vol. 12, no. 1, pp. 37-49, 2019.

[17] T. Wang, C. Ruf, B. Block, D. McKague, and S. Gleason, "Design and Performance of a GPS Constellation Power Monitor System for Improved CYGNSS L1B Calibration," IEEE Journal of Selected Topics in Applied Earth Observation and Remote Sensing, vol. 12, no. 1, pp. 26-36, 2019.

[18] D. Pascual, H. Park, R. Onrubia, A. Alonso-Arroyo, J. Querol, and A. Camps, "Crosstalk Statistics and Impact in Interferometric GNSS-R," IEEE Journal of Selected Topics in Applied Earth Observation and Remote Sensing, vol. 9, no. 10, pp. 4621-4630, 2016.

[19] J. Querol, A. Alonso-Arroyo, R. Onrubia, D. Pascual, H. Park, and A. Camps "SNR Degradation in GNSS-R Measurements Under the Effects of Radio-Frequency Interference," IEEE Journal of Selected Topics in Applied Earth Observation and Remote Sensing, vol. 9, no. 10, pp. 4865-4878 2016.

[20] J. Wickert et al. "GEROS-ISS: GNSS REflectometry, Radio Occultation, and Scatterometry Onboard the International Space Station," IEEE Journal of Selected Topics in Applied Earth Observations and Remote Sensing, vol. 9, no. 10, pp. 4552-4581, 2020.

[21] E. Cardellach, J. Wickert, R. Baggen, J. Benito, A. Camps, N. Catarino, B. Chapron, A. Dielacher, F. Fabra, G. Flato, H. Fragner, C. Gabarro, C. Gommenginger, C. Hass, S. Healy, M. Hernandez-Pajares, P. Hoeg, A. Jaggi, J. Kainulainen, S.A. Khan, N. Lemke, W. Li, Son Nghiem, N. Pierdicca, M. Portabella, K. Rautiainen, A. Rius, I. Sasgen, M. Semmling, C.K. Shum, F. Soulat, A. K. Steiner, S. Tailhades, M. Thomas, R. Vilaseca, and C. Zuffada, "GNSS Transpolar Earth Reflectometry exploriNg System (G-TERN): Mission Concept," IEEE Access, vol. 6, pp. 13980-14018, 2018

[22] M. Martiin-Neira, W. Li, A. Andres-Beivide, and X. Ballesteros-Sels "Cookie: A Satellite Concept for GNSS Remote Sensing Constellations," IEEE Transactions on Geoscience and Remote Sensing, vol. 9, no. 10, pp. 4593-4610, 2016.

[23] A. Rius, O. Nogues-Correig, S. Ribo, E. Cardellach, S. Oliveras, E. Valencia, H. Park, J. Miguel Tarongi, A. Camps, H. van der Marel, R. van Bree, B. Altena, and M. Martin-Neira. "Altimetry with GNSS-R Interferometry: First Proof of Concept Experiment.," GPS Solutions, vol. 16, no. 2, pp. 231-241, 2012.

[24] E. Cardellach, A. Rius, M. Martin-Neira, F. Fabra, O. Nogues-Correig, S. Ribo, J. Kainulainen, A. Camps, and S. D Addio, "Consolidating the Precision of Interferometric GNSS-R Ocean Altimetry Using Airborne Experimental Data," IEEE Transactions on Geoscience and Remote Sensing, vol. 52, no. 8, pp. 4992-5004, 2013.

[25] F. Fabra, E. Cardellach, S. Ribo, W. Li, A. Rius, J. Arco-Fernández, O. Nogues-Correig, J. Praks, E. Rouhe, J. Seppänen, and M. Martin-Neira, "Is Accurate Synoptic Altimetry Achievable by Means of Interferometric GNSS-R?," MDPI Remote Sensing, vol. 11, no. 5, pp. 505, 2019.

[26] R. Onrubia, D. Pascual, J. Querol, H. Park, and A. Camps, "The Global Navigation Satellite Systems Reflectometry (GNSS-R) Microwave Interferometric Reflectometer: Hardware, Calibration, and Validation Experiments," MDPI Sensors, vol. 19, no. 5, pp. 1019, 2019.

[27] H. Carreno-Luengo, A. Camps, I. Ramos-Perez, and A. Rius, "Experimental Evaluation of GNSS-Reflectometry Altimetric Precision Using the P(Y) and C/A Signals," IEEE Journal of Selected Topics in Applied Earth Observation and Remote Sensing, vol. 7, no. 5, pp. 1493-1500, 2014.

[28] S.T. Lowe, T. Meehan, and L. Young, "Direct Signal Enhanced Semicodeless Processing of GNSS Surface-Reflected Signals," IEEE Journal of Selected Topics in Applied Earth Observation and Remote Sensing, vol. 7, no. 5, pp. 1469-1472, 2014.

[29] W. Li, D. Yang, S. D'Addio, and M. Martin-Neira, "Partial Interferometric Processing of Reflected GNSS Signals for Ocean Altimetry," IEEE Geoscience and Remote Sensing Letters, vol. 11, no. 9, pp. 1509-1513, 2015.

[30] H. Park, E. Valencia, A. Camps, A. Rius, S. Ribo, and M. Martin-Neira, "Delay Tracking in Spaceborne GNSS-R Ocean Altimetry," IEEE Geoscience and Remote Sensing Letters, vol. 10, no. 1, pp. 57-61, 2013.

[31] H. Park, D. Pascual, A. Camps, F. Martin, A. Alonso-Arroyo and H. Carreno-Luengo, "Analysis of Spaceborne GNSS-R Delay-Doppler Tracking," IEEE Journal of Selected Topics in Applied Earth Observations and Remote Sensing, vol. 7, no. 5, pp. 1481-1492, 2014.

[32] S. Gleason, S. Hodgart, Y. Sun, C. Gommenginger, S. Mackin, M. Adjrad, and M. Unwin, "Detection and Processing of Bistatically Reflected GPS Signals from Low Earth Orbit for the Purpose of Ocean Remote Sensing," IEEE Transactions on Geoscience and Remote Sensing, vol. 43, no. 6, pp. 1229-1241, 2005.

[33] M. Unwin, P. Jales, J. Tye, C. Gommenginger, G. Foti, and J. Rosello, "Spaceborne GNSS-Reflectometry on TechDemoSat-1: Early Mission Operations and Exploitation," IEEE Journal of Selected Topics in Applied Earth Observation and Remote Sensing, vol. 9, no. 10, pp. 4525-4539, 2014.

[34] H. Carreno-Luengo, A. Camps, P. Vila, J.F. Munoz, A. Cortiella, D. Vidal, J. Jane, N. Catarino, M. Hagenfeldt, P. Palomo, and S. Cornara, "^{3}Cat-2; an Experimental Nano-Satellite for GNSS-R Earth Observation: Mission Concept and Analysis," IEEE Journal of Selected Topics in Applied Earth Observations and Remote Sensing, vol. 9, no. 10, pp. 4540-4551, 2016.

[35] H. Carreno-Luengo, S.T. Lowe, C. Zuffada, S. Esterhuizen, S. Oveisgharan, "Spaceborne GNSS-R from the SMAP mission: First Assessment of Polarimetric Scatterometry over Land and Cryosphere," MDPI Remote Sensing, vol. 9, no. 4, pp. 362, 2017.

[36] C. Jing, X. Niu, C. Duan, F. Lu, G. Di, and Xiaofeng Yang, "Sea Surface Wind Speed Retrieval from the First Chinese GNSS-R Mission: Technique and Preliminary Results," MDPI Remote Sensing, vol. 11, no. 24, pp. 3013, 2019.

[37] D. Masters, "Design and Planning for the First Spire GNSS-R Missions of 2019," in Proc. of the 2019 IEEE GRSS, Specialist Meeting on Reflectometry using GNSS and other Signals of Opportunity, Benevento, Italy, May 2019.

[38] Y. Sun, X. Wang, Q. Du, W. Bai, J. Xia, Y. Cai, D. Wang, C. Wu, X. Meng, Y. Tian, Y. Tian, C. Liu, W. Li, D. Zhao, F. Li, and H. Qiao, "The Status and Progress of Fengyun-3e GNOS II Mission for GNSS Remote Sensing," in Proc. of the 2019 IEEE IGARSS, pp. 5181-5184, Yokohama, Japan, July 2019.

[39] A. Camps, A. Golkar, A. Gutierrez, J.A. Ruiz de Azua, J.F. Munoz-Martin, L. Fernandez, C. Diez, A. Aguilella, S. Briatore, R. Akhtyamov, and N. Garzaniti, "FSSCAT, the 2017 Copernicus Masters' "ESA Sentinel Small Satellite Challenge" Winner: A Federated Polar and Soil Moisture Tandem Mission Based on 6U Cubesats," in Proc. of the 2018 IEEE IGARSS, pp. 8285-8287, Valencia, Spain, July 2018.

[40] J.F. Munoz-Martin, N. Miguelez, R. Castella, L. Fernandez, A. Solanellas, P. Via, and A. Camps, "3Cat-4: Combined GNSS-R, L-Band Radiometer with RFI Mitigation, and AIS Receiver for a 1-Unit Cubesat Based on Software Defined Radio," in Proc. of the 2018 IEEE IGARSS, pp. 1063-1066, Valencia, Spain, July 2018.

[41] A. Dielacher, H. Fragner, M. Moritsch, Per Høeg, J. Wickert, E. Cardellach, O. Koudelka, P. Beck, R. Walker, M. Martin-Neira, and F.P. Lissi, "The Passive Reflectometer on Board of PRETTY," in Proc. of the 2019 ESA ARSI+KEO Conference, The Netherlands, November 2019.

[42] J.C. Juang, S.H. Ma, and C.T. Lin, "Study of GNSS-R Techniques for FORMOSAT Mission," IEEE Journal of Selected Topics in Applied Earth Observations and Remote Sensing, vol. 9, no. 10, pp. 4582-4592, 2016.

[43] A. Helm, O. Montenbruck, J. Ashjaee, S. Yudanov, G. Beyerle, R. Stosius, and M. Rothacher, "GORS - A GNSS Occultation, Reflectometry and Scatterometry Space Receiver," in Proc. of the ION-GNSS-2007 Conference, Fort Worth, TX, USA, September 2007.

[44] A. Helm, "Ground-based GPS Altimetry with the L1 OpenGPS Receiver Using Carrier Phase-Delay Observations of Reflected GPS Signals," Technical Report STR 08/10, Deutsches GeoForschungsZentrum GFZ, Berlin, Germany, 2008.

[45] M. Unwin, J. Pales, P. Blunt, S. Duncan, M. Brummitt, and C. Ruf, "The SGR-ReSI and its Application for GNSS Reflectometry on the NASA EV2 CYGNSS mission," in Proc of the IEEE Aerosp. Conf., Big Sky, MT, USA, March 2013.

[46] C. Ruf, R. Backhus, T. Butler, C.C. Chen, S. Gleason, E. Loria, D. McKague, R. Miller, A. O'Brien, and L. van Nieuwstadt, "Next Generation GNSS-R Instrument," in Proc. of the 2020 IEEE IGARSS, Hawaii, USA, September 2020.

[47] E. Motte, M. Zribi, P. Fanise, A. Egido, J. Darrozes, A. Al-Yaari, N. Baghdadi, F. Baup, S. Dayau, R. Fieuzal, P.-L. Frison, D. Guyon, and J.-P. Wigneron, "GLORI: A GNSS-R Dual Polarization Airborne Instrument for Land Surface Monitoring," MDPI Sensors, vol. 16, no. 5, pp. 732, 2016.

[48] O. Nogues-Correig, E. Cardellach, J. Sanz, and A. Rius, "A GPS Reflections Receiver that Computes Doppler/Delay Maps in Real Time," IEEE Transactions on Geoscience and Remote Sensing, vol. 45, no. 1, pp. 156-174, 2007.

[49] A. Rius, F. Fabra, S. Ribo, J.C. Arco, S. Oliveras, E. Cardellach, A. Camps, O. Nogues-Correig, J. Kainulainen, E. Rohue, and M. Martin-Neira, "PARIS Interferometric Technique Proof of Concept: Sea Surface Altimetry Measurements," in Proc. of the 2012 IEEE IGARSS, pp. 7067-7070, Munich, Germany, July 2012.

[50] S. Ribo, J.C. Arco-Fernandez, E. Cardellach, F. Fabra, W. Li, O. Nogues-Correig, A. Rius, and M. Martin-Neira, "A Software-Defined GNSS Reflectometry Recording Receiver with Wide-Bandwidth, Multi-Band Capability and Digital Beam-Forming," MDPI Remote Sensing, vol. 9, no.5, pp. 450, 2017.

[51] O. Nogues-Correig, "Disseny, Montatge i Validacio d'un Receptor/Gravador de Senyals GPS per a la Demostracio del Concepte PARIS," Proyecto Final de Carrera, Universitat Politecnica de Catalunya, 2002.

[52] O. Nogues-Correig, A. Sumpsi, A. Camps, and A. Rius, "A 3 GPS-Channels Doppler-Delay Receiver for Remote Sensing Applications," in Proc. of the 2003 IEEE IGARSS, pp. 4483-4485, Toulouse, France, September 2003.

[53] N. Rodriguez-Alvarez, X. Bosch-Lluis, A. Camps, M. Vall-llosera, E. Valencia, J.F. Marchan-Hernandez, and I. Ramos-Perez, "Soil Moisture Retrieval Using GNSS-R Techniques: Experimental Results over a Bare Soil Field," IEEE Transactions on Geoscience and Remote Sensing, vol. 47, no. 11, pp. 3616-3624, 2009.

[54] R. Olive, A. Amezaga, H. Carreno-Luengo, H. Park, and A. Camps, "Implementation of a GNSS-R Payload Based on Software-Defined Radio for the ^{3}Cat-2 Mission," IEEE Journal of Selected Topics in Applied Earth Observations and Remote Sensing, vol. 9, no. 10, pp. 4824-4833, 2016.

[55] J.F. Munoz-Martin, L. Fernandez Capon, J.A. Ruiz-de-Azua, and A. Camps, "The Flexible Microwave Payload-2: A SDR-Based GNSS-Reflectometer and L-Band Radiometer for CubeSats," IEEE Journal of Selected Topics in Applied Earth Observations and Remote Sensing, vol. 9, no. 13, pp. 1298-1311, 2010.

[56] C. Ruf, "Mission Update," CYGNSS Science Team Meeting, June 2020.

[57] M. Martin-Neira, M. Caparrini, J. Rossello, S. Lannelongue, and C.S. Vallmitjana, "The PARIS Concept: An Experimental Demonstration of Sea Surface Altimetry Using GPS Reflected Signals," IEEE IEEE Transactions on Geoscience and Remote Sensing, vol. 39, no.1, pp. 142-150, 2001.

[58] S.T. Lowe, C. Zuffada, Y. Chao, P. Kroger, L.E. Young, and J. L. LaBrecque, "5-cm Precision Aircraft Ocean Altimetry Using GPS Reflections," Geophysical Research Letters, vol. 29, no. 10, pp. 1375, 2002.

[59] A. Rius, E. Cardellach, and M. Martin-Neira, "Altimetric Analysis of the Sea-Surface GPS-Reflected Signals," IEEE Transactions on Geoscience and Remote Sensing, vol. 48, no. 4, pp. 2119-2127, 2010.

[60] S. D'Addio, M. Martin-Neira, M. di Bisceglie, C. Galdi, and F. Martin Alemany, "GNSS-R Altimeter Based on Doppler Multi-looking," IEEE Journal of Selected Topics in Applied Earth Observations and Remote Sensing, vol.7, no.5, pp. 1452-1460, 2014.

[61] M. Semmling, T. Schmidt, J. Wickert, S. Schon, F. Fabra, E. Cardellach, and A. Rius, "On the Retrieval of the Specular Reflection in GNSS Carrier Observations for Ocean Altimetry," Radio Science, vol. 47, no. 6, RS6007, 2012.

[62] M. Semmling, J. Beckheinrich, J. Wickert, G. Beyerle, S. Schon, F. Fabra, H. Pflug, K. He, J. Schwabe, and M. Scheinert, "Sea Surface Topography Retrieved from GNSS Reflectometry Phase Data of the GEOHALO Flight Mission," Geophysical Research Letters, vol. 41, no. 3, pp. 954-960, 2014.

[63] M. Semmling, J. Wickert, S. Schon, R. Stosius, M. Markgraf, T. Gerber, M. Ge, and G. Beyerle, G., "A Zeppelin Experiment to Study Airborne Altimetry Using Specular Global Navigation Satellite System Reflections," Radio Science, vol. 48, no. 4, pp. 427-440, 2013.

[64] E. Cardellach, C.O. Ao, M. de la Torre Juarez, and G. A. Hajj, "Carrier Phase Delay Altimetry with GPS-Reflection/Occultation Interferometry from Low Earth Orbiters," Geophysical Research Letters, vol. 31, no. 10, 2004.

[65] W. Li, E. Cardellach, F. Fabra, A. Rius, S. Ribo, and M. Martin-Neira, "First Spaceborne Phase Altimetry over Sea Ice Using TechDemoSat-1 GNSS-R Signals," Geophysical Research Letters, vol. 44, no. 16, pp. 8369-8376, 2017.

[66] E. Cardellach, W. Li, A. Rius, M. Semmling, J. Wickert, F. Zus, C. Ruf, and C. Buontempo, "First Precise Spaceborne Sea Surface Altimetry with GNSS Reflected Signals," IEEE Transactions on Geoscience and Remote Sensing, vol. 13, pp. 102-112, 2020.

[67] M.P. Clarizia, C. Ruf, P. Cipollini, and C. Zuffada, "First Spaceborne Observation of Sea Surface Height Using GPS-Reflectometry," Geophysical Research Letters, vol. 43, no. 2, pp. 767-774, 2016.

[68] W. Li, E. Cardellach, F. Fabra, S. Ribo, and A. Rius, "Assessment of Spaceborne GNSS-R Ocean Altimetry Performance Using CYGNSS Mission Raw Data," IEEE Transactions on Geoscience and Remote Sensing, vol. 58, no. 1, pp. 238-250, 2020.

[69] J. Mashburn, P. Axelrad, C. Zuffada, E. Loria, A. O'Brien, and B. Haines, "Improved GNSS-R Ocean Surface Altimetry with CYGNSS in the Seas of Indonesia," IEEE Transactions on Geoscience and Remote Sensing, pp. 1-17, 2020.

[70] A. Ghavidel, and A. Camps, "Time-Domain Statistics of the Electromagnetic Bias in GNSS-Reflectometry," MDPI Remote Sensing, vol. 7, no. 9, pp. 11151-11162, 2015.

[71] A. Ghavidel, D. Schiavulli, and A. Camps, "Numerical Computation of the Electromagnetic Bias in GNSS-R Altimetry," IEEE Transactions on Geoscience and Remote Sensing, vol. 54, no. 1, pp. 489-498, 2016.

[72] A. Ghavidel, and A. Camps, "Impact of Rain, Swell, and Surface Currents on the Electromagnetic Bias in GNSS-Reflectometry," IEEE Journal of Selected Topics in Applied Earth Observations and Remote Sensing, vol. 9, no. 10, pp. 4643-4649, 2016.

[73] F. Martin, A. Camps, H. Park, S. D'Addio, M. Martin-Neira and D. Pascual, "Cross-Correlation Waveform Analysis for Conventional and Interferometric GNSS-R Approaches," IEEE Journal of Selected Topics in Applied Earth Observations and Remote Sensing, vol. 7, no. 5, pp. 1560-1572, 2014.

[74] S.J. Katzberg, R.A. Walker, J.H. Roles, T. Lynch, and P.G. Black, "First GPS Signals Reflected from the Interior of a Tropical Storm: Preliminary Results from Hurricane Michael," Geophysical Research Letters, vol. 28, no. 10, pp. 1981-1984, 2001.

[75] J.L. Garrison, A. Komjathy, V.U. Zavorotny, and S.J. Katzberg, "Wind Speed Measurement Using Forward Scattered GPS Signals," IEEE Transactions on Geoscience and Remote Sensing, vol. 40, no. 1, pp. 50-75, 2002.

[76] E. Cardellach, G. Ruffini, D. Pino, A. Rius, A. Komjathy, and J.L. Garrison, "Mediterranean Balloon Experiment: Ocean Wind Speed Sensing from the Stratosphere Using GPS Reflections," Remote Sensing Environment, vol. 88, no.3, pp. 351-362, 2003.

[77] O. Germain, G. Ruffini, F. Soulat, M. Caparrini, B. Chapron, and P. Silvestrin, "The Eddy Experiment: GNSS-R Speculometry for Directional Sea Roughness Retrieval from Low Altitude Aircraft," Geophysical Research Letters, vol. 31, no. 21, L21307, 2004.

[78] M.P. Clarizia, C. Gommenginger, S. Gleason, M. Srokosz, C. Galdi, and M. Di Bisceglie, "Analysis of GNSS-R Delay Doppler Maps from the UK-DMC Satellite over the Ocean," Geophysical Research Letters, vol. 36, no. 2, 2009.

[79] V.U. Zavorotny, and A. G. Voronovich, "Scattering of GPS Signals from the Ocean with Wind Remote Sensing Application," IEEE Transactions on Geoscience and Remote Sensing, vol. 38, no. 2, pp. 951-964, 2000.

[80] T. Elfouhaily, D.R. Thompson, and L. Linstrom, "Delay-Doppler Analysis of Bistatically Reflected Signals from the Ocean Surface: Theory and Application," IEEE Transactions on Geoscience and Remote Sensing, vol. 40, no. 3, pp. 560-573, 2002.

[81] S. Gleason, "Remote Sensing of Ocean, Ice, and Land surfaces Using Bistatically Scattered GNSS Signals from Low Earth Orbit," Ph.D. Thesis, University of Surrey, United Kingdom, 2006.

[82] A. Camps, M. Caparrini, R. Sabia, and G. Ruffini, "Sea Surface Salinity Retrieval from Space: Potential Synergetic Use of GNSS-R Signals to Improve the Sea State Correction and Application to the SMOS Mission," in Proc. IEEE Microwave Radiometry and Remote Sensing of the Environment (MicroRad 2006), February 2006.

[83] J.F. Marchan-Hernandez, N. Rodriguez-Alvarez, A. Camps, X. Bosch-Lluis, I. Ramos-Perez, and E. Valencia, "Correction of the Sea State Impact in the L-band Brightness Temperature by Means of Delay Doppler Maps of Global Navigation Satellite Signals Reflected over the Sea Surface," IEEE Transactions on Geoscience and Remote Sensing, vol. 46, no. 1, pp. 2914-2923, 2008.

[84] E. Valencia, A. Camps, N. Rodriguez-Alvarez, I. Ramos-Perez, X. Bosch-Lluis, and H. Park, "Improving the Accuracy of Sea Surface Salinity Retrieval Using GNSS-R Data to Correct the Sea State Effect," Radio Science, vol. 46, no. 6, pp. RS0C02, 2011.

[85] E. Cardellach and A. Rius, "A New Technique to Sense Non-Gaussian Features of the Sea Surface from L-Band Bi-Static GNSS Reflections,". Remote Sensing of Environment, vol. 112, no. 6, pp. 2927-2937, 2008.

[86] E. Valencia, A. Camps, J. F. Marchan-Hernandez, H. Park, X. Bosch-Lluis, N. Rodriguez-Alvarez, and I. Ramos-Perez, "Ocean Surface's Scattering Coefficient Retrieval by Delay Doppler Map Inversion," IEEE Geoscience and Remote Sensing Letters, vol. 8, no. 4, pp. 750-754, 2011.

[87] G. Schiavulli, D. Nunziata, F. Pugliano and M. Migliaccio, "Reconstruction of the Normalized Radar Cross Section field from GNSS-R Delay Doppler Map," IEEE Journal of Selected Topics in Applied Earth Observations and Remote Sensing, vol. 7, no. 5, pp. 573-1583, 2014.

[88] G. Foti, C. Gommenginger, P. Jales, M. Unwin, A. Shaw, C. Robertson, and J. Rosello, "Spaceborne GNSS Reflectometry for Ocean Winds: First Results from the UK TechDemoSat-1 Mission," Geophysical Research Letters, vol. 42, no. 13, 2015.

[89] B. Annane, B. McNoldy, S. Leidner, R. Hoffman, R. Atlas, and S. Majumdar, "A Study of the HWRF Analysis and Forecast Impact of Realistically Simulated CYGNSS Observations Assimilated as Scalar Wind Speeds and as VAM Wind Vectors," Monthly Weather Rev., vol. 146, no. 7, pp. 26-36, 2018.

[90] S. Leidner, B. Annane, B. McNoldy, R. Hoffman, and R. Atlas, "Variational Analysis of Simulated Ocean Surface Winds from the CYclone Global Navigation Satellite System (CYGNSS) and Evaluation Using a Regional OSSE," Journal of Atmospheric and Oceanic Technology, vol. 35, no. 8, pp. 1571-1584, 2018,

[91] Z. Cui, Z. Pu, V. Tallapragada, R. Atlas, and C.S. Ruf, "Impact of CYGNSS Ocean Surface Wind Speeds on Numerical Simulations of Hurricanes Harvey and Irma (2017)," Geophysical Research Letters, vol. 46, no. 5, pp. 2984-2992, 2019.

[92] D. Mayers, and C.S. Ruf, "Tropical Cyclone Center Fix Using CYGNSS Winds," Journal of Applied Meteorology and Climatology, vol. 58, no. 9, pp. 1993-2003, 2019.

[93] M.P. Clarizia, and C.S. Ruf, "Wind Speed Retrieval Algorithm for the Cyclone Global Navigation Satellite System (CYGNSS) Mission," IEEE Transactions on Geoscience and Remote Sensing, vol. 54, no. 8, pp. 4419-4432, 2016.

[94] C.S. Ruf et al., "New Ocean Winds Satellite Mission to Probe Hurricanes and Tropical Convection," Bull. Amer. Meteorolog. Soc., vol. 97, no. 3, pp. 385-395, 2016.

[95] C. Ruf and R. Balasubramaniam, "Development of the CYGNSS Geophysical Model Function for Wind Speed," IEEE Journal of Selected Topics in Applied Earth Observations and Remote Sensing, vol. 12, no. 1, pp. 66-77, Jan. 2019.

[96] C. Ruf et al., "In-Orbit Performance of the Constellation of CYGNSS Hurricane Satellites," Bull. Amer. Meteorolog. Soc., vol. 100, no. 10, pp. 1-46, 2019.

[97] S. Gleason, C.S. Ruf, A. O'Brien, and D.S. McKague, "The CYGNSS level 1 Calibration Algorithm and Error Analysis Based on On-Orbit Measurements," IEEE Journal of Selected Topics in Applied Earth Observations and Remote Sensing, vol. 12, no. 1, pp. 37-49, Jan. 2019.

[98] J. Reynolds, M.P. Clarizia, and E. Santi, "Wind Speed Estimation from CYGNSS Using Artificial Neural Networks," IEEE Journal of Selected Topics in Applied Earth Observations and Remote Sensing, vol. 13, pp. 708 -716, 2020.

[99] M.P. Clarizia, "Investigating the Effect of Ocean Waves on GNSS-R Microwave Remote Sensing Measurements," Ph.D. dissertation, School of Ocean Earth Sci., Univ. Southampton, Southampton, U.K., 2012.

[100] H. Carreno-Luengo, A. Camps, I. Ramos-Perez, G. Forte, R. Onrubia, and R. Diez, "^{3}Cat-2: A P(Y) and C/A GNSS-R Experimental Nano-Satellite Mission," in Proc. of the 2013 IEEE IGARSS, pp. 843-846, Melbourne, Australia, July 2013.

[101] H. Carreno-Luengo, and A. Camps, "Empirical Results of a Surface Level GNSS-R Experiment in a Wave Channel," MDPI Remote Sensing, vol. 7. no. 6, pp. 7471-7493, 2015.
[102] S. Soisuvarn, Z. Jelenak, F. Said, P. S. Chang, and A. Egido, "The GNSS Reflectometry Response to the Ocean Surface Winds and Waves," IEEE Journal of Selected Topics in Applied Earth Observations and Remote Sensing, vol. 9, no. 10, pp. 4678-4699, 2016.
[103] J.F. Munoz-Martin, R. Onrubia, D. Pascual, H. Park, A. Camps, C. Rudiger, J. Walker, and A. Monerris, "Untangling the Incoherent and Coherent Scattering Components in GNSS-R and Novel Applications," MDPI Remote Sensing, vol. 12, no. 7, pp. 1018, 2020.
[104] J.F. Munoz-Martin, R. Onrubia, D. Pascual, H. Park, A. Camps, C. Rudiger, J. Walker, and A. Monerris, "Experimental Evidence of Swell Signatures in Airborne L5/E5a GNSS-Reflectometry," MDPI Remote Sensing, vol. 12, no. 11, pp. 1759, 2020.
[105] B. Li, L. Yang, B. Zhang, D. Yang, and Di Wu, "Modeling and Simulation of GNSS-R Observables with Effects of Swell," IEEE Journal of Selected Topics in Applied Earth Observations and Remote Sensing, vol. 13, pp. 1833-1841, 2020.
[106] G. Carrie, T. Deloues, J. Mametsa, and S. Angelliaume, "Ship Detection Based on GNSS Reflected Signals: An Experimental Plan," in Proc. of Space Reflecto, Calais, France, 2011.
[107] M.P. Clarizia, P. Braca, C.S. Ruf, and P. Willett, "Target Detection Using GPS Signals of Opportunity," in Proc. of the 18th Int. Conf. Inf. Fusion, pp. 1429-1436, Washington, DC, USA, 2015.
[108] W. Ji, C. Xiu, W. Li, and L. Wang, "Ocean Surface Target Detection and Positioning Using the Spaceborne GNSS-R Delay-Doppler Maps," in Proc. of the IEEE IGARSS, pp. 3806–3809, Quebec City, QC, Canada, 2014.
[109] Y. Lu, D. Yang, W. Li, J. Ding, and Z. Li, "Study on the New Methods of Ship Object Detection Based on GNSS Reflection," Marine Geodesy, vol. 32, no. 1, pp. 22–30, 2013.
[110] A. Di Simone, H. Park, D. Riccio, and A. Camps, "Sea Target Detection Using Spaceborne GNSS-R Delay-Doppler Maps: Theory and Experimental Proof of Concept Using TDS-1 Data," IEEE Journal of Selected Topics in Applied Earth Observation and Remote Sensing, vol. 10, no. 9, pp. 4537-4255, 2017.
[111] B.J. Southwell, J.W. Cheong, and A.G. Dempster, "A Matched Filter for Spaceborne GNSS-R Based Sea-Target Detection," IEEE Transactions on Geoscience and Remote Sensing, vol. 58, no. 8, pp. 5922 -5931, 2020.
[112] T. Beltramont, P. Braca, M. Di Bisceglie, A. Di Simone, C. Galdi, A. Iodice, L.M. Millefiori, D. Riccio, and P. Willett, "Simulation-Based Feasibility Analysis of Ship Detection Using GNSS-R Delay-Doppler Maps," IEEE Journal of Selected Topics in Applied Earth Observation and Remote Sensing, vol. 10, no. 9, pp. 4537-4255, 2020.
[113] D. Masters, V.U. Zavorotny, S. Katzsberg, and W. Emery, "GPS Signal Scattering from Land for Moisture Content Determination," in Proc. of the 2000 IEEE IGARSS, pp. 3090-3092, Honolulu, USA, July 2000.
[114] A. Egido, C. Martin-Puig, D. Felip, M. Garcia, M. Caparrini, E. Farres, and G. Ruffini, "The SAM Sensor: An Innovative GNSS-R System for Soil Moisture Retrieval," in Proc. of the NAVITEC Conference, European Space and Technology Centre ESTEC/ESA, Noordwijk, The Netherlands, April 2008.
[115] S.J. Katzberg, O. Torres, M.S. Grant, and D. Masters, "Utilizing Calibrated GPS Reflected Signals to Estimate Soil Reflectivity and Dielectric Constant: Results from SMEX02," Remote Sensing of the Environment, vol. 100, no.1, pp. 17-28, 2006.
[116] N. Pierdicca, L. Guerriero, R. Giusto, M. Brogioni, and A. Egido, "SAVERS: A Simulator of GNSS Reflections from Bare and Vegetated Soils," IEEE Transactions on Geoscience and Remote Sensing, vol. 52, no. 10, pp. 6542-6554, 2014.
[117] V.U. Zavorotny, K.M. Larson, J.J. Braun, E.E. Small, E.D. Gutmann, and A.L. Bilich, "A Physical Model for GPS Multipath Caused by land Reflections: Toward Bare Soil Moisture Retrievals," IEEE Journal of Selected Topics in Applied Earth Observations and Remote Sensing, vol. 3, no. 1, pp. 100-110, 2010.
[118] K.M. Larson, E.E. Small, E. Gutmann, A. Bilich, P. Axelrad, and J. Braun, "Using GPS Multipath to Measure Soil Moisture Fluctuations: Initial results," GPS Solutions, vol. 12, pp. 173-177, 2008.
[119] A. Alonso-Arroyo, A. Camps, A. Aguasca, G. Forte, A. Moneris, C. Rudiger, J.P. Walker, H. Park, D. Pascual, and R. Onrubia, "Dual-Polarization GNSS-R Interference Pattern Technique for Soil Moisture Mapping," IEEE Transactions on Geoscience and Remote Sensing, vol. 7, no. 5, pp. 1533-1544, 2014.
[120] A. Egido, S. Paloscia, E. Motte, L. Guerriero, N. Pierdicca, M. Vaparrini, E. Santi, G. Fontanelli, and N. Floury, "Airborne GNSS-R Polarimetric Measurements for Soil Moisture and Above Ground Biomass Estimation," IEEE Journal of Selected Topics in Applied Earth Observations and Remote Sensing, vol. 7, no. 5, pp. 1522-1532, 2014.
[121] E. Motte, M. Zribi, P. Fanise, A. Egido, J. Darrozes, A. Al-Yaari, N. Baghdadi, F. Baup, S. Dayau, R. Fieuzal, P.-L. Frison, D. Guyon, and J.-P. Wigneron, "GLORI: A GNSS-R Dual Polarization Airborne Instrument for Land Surface Monitoring," MDPI Sensors vol. 16, no. 5, pp. 732, 2016.
[122] E.E. Small, M.L. Kristine, C.C. Chew, J. Dong, and T.E. Ochsner, "Validation of GPS-IR Soil Moisture Retrievals: Comparison of Different Algorithms to Remove Vegetation Effects," IEEE Transactions on Geoscience and Remote Sensing, vol. 9, no. 10, pp. 4759-4770, 2016.
[123] A. Camps, H. Hyuk, M. Pablos, G. Foti, C. Gommerginger, P.W. Liu, and J. Judge, "Sensitivity of GNSS-R spaceborne observations to soil moisture and vegetation," IEEE Journal of Selected Topics in Applied Earth Observations and Remote Sensing, vol. 9, no. 10, pp. 4730-4732, 2016.
[124] C. Chew, R. Shah, C. Zuffada, G. Hajj, D. Masters, and A.J. Mannucci, "Demonstrating Soil Moisture Remote Sensing with Observations from the UK TechDemoSat-1 Satellite Mission," Geophysical Research Letters, vol. 43, no. 7, pp. 3317-3324, 2016.
[125] M. Piles, D. Entekhabi, A.G. Konings, K.A. McColl, N.N. Das, and T. Jagdhuber, "Multi-temporal Microwave Retrievals of Soil Moisture and Vegetation Parameters from SMAP," in Proc. of the 2016 IEEE IGARSS, pp. 202-245, Beijing, China, July 2016.
[126] C. Chew, and E.E. Small, "Soil Moisture Sensing Using Spaceborne GNSS Reflections: Comparison of CYGNSS reflectivity to SMAP soil moisture," Geophysical Research Letters, vol. 45, no. 9, pp. 4049-4057, 2018.
[127] H. Carreno-Luengo, G. Luzi, and M. Crosetto, "Impact of the Elevation Angle on CYGNSS GNSS-Bistatic Reflectivity," MDPI Remote Sensing, vol. 10, no. 11. pp. 1-21, 2018.
[128] A. Camps, M. Vall-llosera, H. Park, G. Portal, L. Rossato, "Sensitivity of TDS-1 Reflectivity to Soil Moisture: Global and Regional Differences and Impact of Different Spatial Scales," MDPI Remote Sensing, vol. 10, no. 11, pp. 1856, 2018
[129] M.M. Al-Khaldi, J. T. Johnson, A. J. O'Brien, A. Balenzano, and F. Mattia, "Time-Series Retrieval of Soil Moisture Using CYGNSS," IEEE Transactions on Geoscience and Remote Sensing, vol. 57, no. 7, pp. 4322-4331, 2019.
[130] M.P. Clarizia, N. Pierdicca, F. Costantini, and N. Floury, "Analysis of CYGNSS Data for Soil Moisture Retrieval," IEEE Journal of Selected Topics in Applied Earth Observations and Remote Sensing, vol. 12, no. 7, pp. 2227-2235, 2019.
[131] C. Chew, and E. Small, "Description of the UCAR/CU Soil Moisture Product," MDPI Remote Sensing, vol. 12, no. 10, pp. 1558, 2020.
[132] A. Camps, H. Park, J. Castellvi, J. Corbera, and E. Ascaso, "Single-Pass Soil Moisture Retrievals Using GNSS-R: Lessons Learned," MDPI Remote Sensing, vol. 12, no. 12, pp. 2064, 2020.
[133] H. Park, A. Camps, J. Castellvi, and J. Muro, "Generic Performance Simulator of Spaceborne GNSS-Reflectometer for Land Applications," IEEE Journal of Selected Topics in Applied Earth Observations and Remote Sensing, vol. 13, pp. 3179-3191, 2020.
[134] P. Liang, L.E. Pierce, and M. Moghaddam, "Radiative Transfer Model for Microwave Bistatic Scattering from Forests Canopies," IEEE Transactions on Geoscience and Remote Sensing, vol. 43, no. 11, pp. 2470-2483, 2005.
[135] P. Ferrazzoli, L. Guerriero, N. Pierdicca, and R. Rahmoune, "Forest Biomass Monitoring with GNSS-R: Theoretical Simulations," Advances in Space Research, vol. 47, no. 10, pp. 1823-1832, 2011.
[136] X.R. Wu, and S.J. Jin, "GPS-Reflectometry: Forest Canopies Polarization Scattering Properties and Modelling," Advances in Space Research, vol. 54, no. 5, pp. 863-870, 2014.
[137] A. Egido, "GNSS Refectometry for Land Remote Sensing Applications," Ph.D. Thesis, Universitat Politecnica de Catalunya (UPC),

Barcelona, Spain, 2013. Online available https://tdx.cat/handle/10803/129090 (accessed 1 May 2020)

[138] H. Carreno-Luengo, "Contributions to GNSS-R Earth Remote Sensing from Nano-Satellites," Ph.D. Thesis, Universitat Politecnica de Catalunya (UPC), Barcelona, Spain, 2016. Online available https://www.tdx.cat/handle/10803/385216 (accessed 1 May 2020)

[139] H. Carreno-Luengo, A. Amezaga, D. Vidal, R. Olive, J.F. Munoz, and A. Camps, "First Polarimetric GNSS-R Measurements from a Stratospheric Flight over Boreal Forests," MDPI Remote Sensing, vol. 7, no. 10, pp. 13120-13138, 2015

[140] M. Kurum, M. Deshpande, A.T. Joseph, P.E. O'Neill, R.H. Lang, and O. Eroglu, "SCoBi-Veg: A Generalized Bistatic Scattering Model of Reflectometry from Vegetation for Signals of Opportunity Applications," IEEE Transactions on Geoscience and Remote Sensing, vol. 57, NO. 2, pp. 1049-1068, 2018.

[141] A. Lindermayer, "Developmental Algorithms for Multicellular Organisms: A Survey of L-Systems," J. Theor. Bio., vol. 54, 3-22, 1975

[142] L. Tsang, J.A. Kong, and R.T. Shin, "Theory of Microwave Remote Sensing," Wiley Interscience: New York, NY, USA, 1985.

[143] M. Zribi, D. Guyon, E. Motte, S. Dayau, J.P. Wigneron, N. Baghdadi, and N. Pierdicca, "Performance of GNSS-R GLORI Data for Biomass Estimation over the Landes Forests," Elsevier International Journal of Applied Earth Observation and Geoinformation, vol. 74, pp. 150-158, 2019.

[144] H. Carreno-Luengo, G. Luzi, and M. Crosetto, "Above-Ground Biomass Retrieval over Tropical Forests: A Novel GNSS-R Approach with CYGNSS," MDPI Remote Sensing, vol. 12, no. 9, pp. 1368, 2020.

[145] A. Camps, A. Alonso-Arroyo, H. Park, R. Onrubia, D. Pascual, and J. Querol, "L-Band Vegetation Optical Depth Estimation Using Transmitted GNSS Signals: Application to GNSS-Reflectometry and Positioning," MDPI Remote Sensing, vol. 12, no. 15, pp. 2352, 2020.

[146] S.V. Nghiem, C. Zuffada, R. Shah, C. Chew, S.T. Lowe, A.J. Mannucci, E. Cardellach, G.R. Brakenridge, G. Geller, and A. Rosenqvist, "Wetland Monitoring with Global Navigation Satellite System Reflectometry," Earth and Space Science, vol. 4, no. 1, pp. 16–39, 2017.

[147] C. Chew, J.T. Reager, and E. Small, E., "CYGNSS Data Map Flood Inundation During the 2017 Atlantic Hurricane Season," Scientific Reports, vol. 8. pp. 1-8.

[148] C. Gerlein-Safdi, and C.S. Ruf, "A CYGNSS-Based Algorithm for the Detection of Inland Waterbodies," Geophysical Research Letters, vol. 46, pp. 12065-12072, 2019.

[149] M. Morris, C. Chew, J.T. Reager, R. Shah, and C. Zuffada, "A Novel Approach to Monitoring Wetland Dynamics Using CYGNSS: Everglades Case Study," Remote Sensing of the Environment, vol. 23, 2019.

[150] M. M. Al-Khaldi, J. T. Johnson, S. Gleason, C.C. Chew, C. Gerlein-Safdi, R. Shah, and C. Zuffada "Inland Water Body Mapping Using CYGNSS Coherence Detection," IEEE Transactions on Geoscience and Remote Sensing, 2021.

[151] M. Wiehl, B. Legresy, and R. Dietrich, "Potential of Reflected GNSS Signals for Ice Sheet Remote Sensing," Progress in Electromagnetics Research, vol. 40, pp. 177-205, 2003.

[152] K.M. Larson, E.D. Gutmann, V.U. Zavorotny, J.J. Braun, M.W. Williams, and F.G. Nievinski, "Can We Measure Snow Depth with GPS Receivers?," Geophysical Research Letters, vol. 36, no. 17, L17502, 2009.

[153] M.D. Jacobson, "Inferring Snow Water Equivalent for a Snow-Covered Ground Reflector Using GPS Multipath Signals," MDPI Remote Sensing, vol. 2, pp. 2426-2441, 2010.

[154] N. Rodriguez-Alvarez, A. Aguasca, E. Valencia, X. Bosch-Lluis, A. Camps, I. Ramos-Perez, H. Park, and M. Vall-llossera, "Snow Thickness Monitoring Using GNSS Measurements," IEEE Geoscience and Remote Sensing Letters, vol. 9, no. 6, pp. 1109-1113, 2011.

[155] M. Semmling, G. Beyerle, R. Stosius, G. Dick, J. Wickert, F. Fabra, E. Cardellach, S. Ribo, A. Rius, A. Helm, S.B. Yudanov, and S. D'Addio, "Detection of Arctic Ocean Tides using Interferometric GNSS-R Signals," Geophysical Research Letters, vol. 38, no. 4, L04103, 2011.

[156] F. Fabra, "GNSS-R as a Source of Opportunity for Remote Sensing of the Cryosphere," Ph.D. Thesis, Universitat Politecnica de Catalunya (UPC), Barcelona, Spain, 2013. Online available https://www.tesisenred.net/handle/10803/117605 (accessed 10 May 2020)

[157] F. Fabra, E. Cardellach, A. Rius, S. Ribo, S. Oliveras, O. Nogues-Correig, M. Belmonte Rivas, M. Semmling, and S. D'Addio, "Phase Altimetry with Dual Polarization GNSS-R over Sea Ice," IEEE Transactions on Geoscience and Remote Sensing, vol. 50, no. 6, pp. 2112-2121, 2011.

[158] A. Komjathy, J. Maslanik, V.U. Zavorotny, P. Axelrad, and S.J. Katzberg, "Sea Ice Remote Sensing Using Surface Reflected GPS Signals," in Proc. of the 2000 IEEE IGARSS, pp. 2855-2857, Honolulu, USA, July 2000.

[159] S. Gleason, "Towards Sea Ice Remote Sensing with Space Detected GPS Signals: Demonstration of Technical Feasibility and Initial Consistency Check Using Low Resolution Sea Ice Information," MDPI Remote Sensing, vol. 2, no. 8, pp. 2017-2039, 2010.

[160] E. Cardellach, F. Fabra, O. Nogues-Correig, S. Oliveras, S. Ribo, and A. Rius, "GNSS-R Ground-Based and Airborne Campaigns for Ocean, Land, Ice and Snow techniques: Application to the GOLD-RTR Datasets," Radio Science, vol. 46, no.6, RS0C04, 2011.

[161] V. Zavorotny, and C. Zuffada, "A Novel Technique for Characterizing the Thickness of First-Year Sea-Ice with the GPS Reflected Signal," Eos Trans. AGU, vol. 83, no. 47, Fall Meet. Suppl., Abstract C11A-0980, 2002.

[162] M. Belmonte, "Bistatic Scattering of Global Positioning System Signals from Arctic Sea Ice," Ph.D. Thesis, University of Colorado, Boulder, CO, USA, 2007.

[163] M. Belmonte, J.A. Maslanik, and P. Axelrad, "Bistatic Scattering of GPS Signals off Arctic Sea Ice," IEEE Transactions on Geoscience and Remote Sensing, vol. 48, no. 3, pp. 1548-1553, 2009.

[164] H. Carreno-Luengo, S. Lowe, C. Zuffada, S. Esterhuizen, and S. Oveisgharan, Advancing GNSS-R Ocean Scatterometry and Altimetry; SMAP + CYGNSS, in Proc. of the 2017 IEEE GRSS Specialist Meeting on Reflectometry using GNSS and other Signals of Opportunity, Ann Arbor, MI, USA, May 2017. Online available http://www.gnssr2017.org/images/Wednesday_morning/GNSS+R2017_WE_AM_2_Carreno-Luengo_SMAP_Scatterometry.pdf (accessed 10 May 2020)

[165] H. Carreno-Luengo, S. Lowe, C. Zuffada, S. Esterhuizen, and S. Oveisgharan, "GNSS-R from the SMAP and CYGNSS Missions: Application to Polarimetric Scatterometry and Ocean Altimetry," in Proc. of the 2017 IEEE IGARSS, pp. 5019-5021, Fort Worth, TX, USA, July 2017.

[166] A. Alonso-Arroyo, V.U. Zavorotny, and A. Camps, "Sea Ice Detection Using U.K. TDS-1 GNSS-R Data," IEEE Transactions on Geoscience and Remote Sensing, vol. 55, no. 9, pp. 4989-5001, 2017.

[167] Q. Yan, and W. Huang, "Sea Ice Sensing From GNSS-R Data Using Convolutional Neural Networks," IEEE Geoscience and Remote Sensing Letters, vol. 15, no. 10, pp. 1510-1514, 2018.

[168] Q. Yan, and W. Huang, "Detecting Sea Ice from TechDemoSat-1 Data Using Support Vector Machines with Feature Selection," IEEE Journal of Selected Topics in Applied Earth Observations and Remote Sensing, vol. 12, no. 5, pp. 1409-1416, 2019.

[169] B.J. Southwell, and A.G. Dempster, "Sea Ice Transition Detection Using Incoherent Integration and Deconvolution," IEEE Journal of Selected Topics in Applied Earth Observations and Remote Sensing, vol. 13, pp. 14-20, 2020.

[170] Q. Yan, W. Huang, "Sea Ice Thickness Measurement Using Spaceborne GNSS-R: First Results with TechDemoSat-1 Data," IEEE Journal of Selected Topics in Applied Earth Observations and Remote Sensing, vol. 13, pp. 577-587, 2020.

[171] Y. Zhu, T. Tao, J. Zou, K. Yu, J. Wickert, and M. Semmling, "Spaceborne GNSS Reflectometry for Retrieving Sea Ice Concentration Using TDS-1 Data," pp. 1-5, IEEE Geoscience and Remote Sensing Letters, 2020.

[172] N. Rodriguez-Alvarez, B. Holt, S. Jaruwatanadilok, E. Podest, and K.C. Cavanaugh, "An Arctic Sea Ice Multi-Step Classification Based on GNSS-R Data from the TDS-1 Mission," Elsevier Remote Sensing of the Environment, vol. 230, 2019.

[173] A. Rius, E. Cardellach, F. Fabra, W. Li, S. Ribo, M. Hernandez-Pajares, "Feasibility of GNSS-R Ice Sheet Altimetry in Greenland Using TDS-1," MDPI Remote Sensing, vol. 9, no. 7, pp. 742, 2017.

[174] W. Li, E. Cardellach, F. Fabra, S. Ribo, and A. Rius, "Measuring Greenland Ice Sheet Melt Using Spaceborne GNSS Reflectometry from TechDemoSat-1," Geophysical Research Letters, vol. 47, no. 2, pp. 1-10, 2020.